Dyes and Pigments 246 (2026) 113390

Contents lists available at ScienceDirect

Dyes and Pigments

journal homepage: www.elsevier.com/locate/dyepig

A dual-signal Mn(II)-MOF fluorescent sensor for detection of water pollutants, food additives, and their induced sweat metabolic biomarkers

Ying Wang [a,b], Bai-gang An [a,*], Lei Guan [b,**]

[a] Key Laboratory of Energy Materials and Electrochemistry Research Liaoning Province, School of Chemical Engineering, University of Science and Technology Liaoning, Anshan, 114051, China
[b] College of Science, Liaoning Petrochemical University, Fushun, 113001, China

ARTICLE INFO

Keywords:
Mn(II)-MOF
Fluorescent sensor
Water pollutant
Food additive
Biomarker

ABSTRACT

5,5'-(diazene-1,2-diyl)bis(2-hydroxybenzoic acid) (H_2L) is used as a ligand precursor for a high-performance metal-organic framework (MOF)-based fluorescent probe, due to its dye characteristic group. The hydrothermal reaction of H_2L and 4, 4'-bipyridine (4,4'-bipy) with Mn(II) salt led to a MOF $Mn_3(L)_4(4,4'\text{-bipy})_2(H_2O)_2\cdot Mn(4,4'\text{-bipy})_2(H_2O)_2\cdot 4H_2O$ (MOF-**1**). MOF-**1** features a 3D net with 1D square channels (12.50 Å × 15.36 Å), where L^{2-} ligands link trinuclear Mn clusters via bis-bridging and bis-monodentate carboxylate groups. MOF-**1** has good chemical stability across a wide pH range and strong blue luminescence. It enables quantitative detection of Fe^{3+}, MnO_4^-, dehydroacetic acid sodium salt (SDH), and hydrocortisone (HC) via fluorescence turn-off effect, and Pb^{2+}, tartaric acid (TA), and ascorbic acid (AA) through fluorescence turn-on effect, with high selectivity, good reusability, and low limits of detection (LODs). The sensing of Fe^{3+} and MnO_4^- involves the competitive absorption (CA) and the resonance energy transfer (RET) mechanisms. The sensing of Fe^{3+} also relies on the weak interactions with uncoordinated O sites in carboxylate groups. The detection of Pb^{2+} primarily relies on its weak interactions with benzene moieties of L^{2-} ligands. Orbital energy theoretical calculations reveal that the fluorescence changes of MOF-**1** for SDH, HC, TA, and AA mainly stem from photoinduced electron transfer (PET). The CA process also plays an important role for SDH detection. The detection of water pollutants in real water samples (tap, spring, and Hunhe River) and of HC and AA in 100-fold diluted real sweat is achieved with corresponding recoveries of 98.00–103.70 %, 100.1 %, and 104.10 %. MOF-**1** fabricated into test strips can rapidly detect HC and AA in sweat. These results highlight the potential of MOF-**1** as a dual-signal sensor for detecting water pollutants and food additives, and for sensing specific sweat biomarkers to evaluate exposure to these substances.

1. Introduction

With the rapid development of industry in modern society comes the inevitable discharge of industrial waste [1], which seriously pollutes rivers [2] and groundwater [3], and migrates in water bodies [4]. Polluted water bodies usually contain various harmful substances, such as heavy metal ions [5], inorganic anions [6], and organic pollutants [7]. These substances can accumulate in the body and cause a series of health problems when ingested by humans over the long term. In addition to the health risks from water pollutants, food additives and food safety have attracted widespread attention [8]. Food additives are widely used in the food industry, which can delay deterioration, improve taste, and enhance color of food. Abuse of food additives may affect the digestive, absorptive, and metabolic functions of the human body, and even cause diseases [9]. Water pollutants and food additives can be regarded as two major "potential killers" to human health. It is important to accurately detect these substances for timely assessing potential hazards.

Human sweat is an important physiological product, containing trace metabolic biomarkers that can directly reflect physiological changes in the human body [10]. Given the health threat of water pollutants and food additives, detecting specific sweat biomarkers is crucial for assessing the impact of these substances on the human body [11].

Since the problems of water pollution and food safety become

* Corresponding author.
** Corresponding author.
E-mail addresses: bgan@ustl.edu.cn (B.-g. An), gl_coord@163.com (L. Guan).

https://doi.org/10.1016/j.dyepig.2025.113390
Received 22 August 2025; Received in revised form 27 September 2025; Accepted 3 November 2025
Available online 4 November 2025

increasingly severe, the demand for health monitoring continues to grow [12]. Designing and preparing a suitable material has accordingly become an urgent task, which not only can detect harmful substances, but also can reflect the physiological changes caused by them via sweat biomarker detection [13]. Metal-organic frameworks (MOFs) is a type of functional materials [14], which can stand out in analytical sensing field due to their topological architectures [15] and structural tunability [16]. Biphenyldicarboxylate ligands are considered as ideal candidates for fabricating MOF-based fluorescent probes due to their strong coordination ability, diverse coordination modes, and good chemical stability to water, acid and base. They have been widely reported for detecting water pollutants, food additives, and biomarkers in body fluids in recent years, showing broad prospects in practical detection. Yang et al. [17] reported a MOF, $[Cd(bpdc)(bbzb)\cdot 2H_2O]_n$, synthesized with 4,4′-biphenyldicarboxylic acid (H_2bpdc) and 4,7-bis(1H-benzimidazol-1-yl)-2,1,3-benzothiazole (bbzb). It can be considered as a good fluorescent sensor for the detection of Al^{3+}, Fe^{3+}, AcO^- and $Cr_2O_7^{2-}$. Its fluorescent test paper has been further developed to realize naked-eye detection of these cations and anions. Li et al. [18] reported a coordination polymer (CP), $[Eu(bpdc)_{0.5}(ppda)(C_2H_5OH)(H_2O)]_n$, synthesized with H_2bpdc and 3-(2,4-dicarboxyphenyl)-6-carboxypyridine (H_2ppda). It was used as a fluorescent sensor for the detection of food additives, such as tartrazine (TA) and folic acid (FA). The LODs reach the 10^{-8} level. Its fabricated film showed remarkable potential for visual recognition of TA and FA. Zhao et al. [19] reported a novel CP, $[Zn_2(bpdc)(typt)_2]\cdot 2H_2O$, synthesized with H_2bpdc and 4-(tetrazol-5-yl)phenyl-4,2′:6′,4″-terpyridine) (typt). It was used as a recyclable fluorescent sensor to detect hippuric acid (HA) in urine for indexing toluene exposure and could be an ideal candidate for practical application as an HA sensor. The molecular design has been applied to the design of biphenyldicarboxylate ligands for further optimizing sensing performance [20]. Three design strategies, namely multiple coordination sites, large conjugated structures, and electron-donating groups, have been validated in related literature: (1) the polycarboxylate groups on their aromatic backbones can form stable coordination bonds with metal ions, thereby constructing complicated topological architectures [21]; (2) introducing an azo or vinylene function into aromatic backbone can effectively expand the conjugated system, and provide more electron transfer pathways, contributing to the improvement of fluorescent sensing performance [22]; (3) aromatic backbones functionalized with amino or hydroxyl groups can enhance the interaction with target analytes and improve the selectivity and sensitivity in detection [23]. Despite the remarkable progress achieved in the construction and improvement of MOF-based fluorescent probes, one key challenge remains unsolved. Most existing probes are designed for single-field detection, making it difficult to meet the demand for cross-field detection in practical scenarios.

H_2L ligand precursor is an excellent building block for constructing a high-performance MOF-based fluorescent probe, which perfectly integrates the above-mentioned all design principles, providing a new way for addressing the challenges in cross-field detection, namely in water pollution detection, food safety monitoring and health assessment. The as-synthesized Mn(II)-MOF functions as a sensitive dual-signal fluorescence probe, detecting water pollutants, food additives, and sweat biomarkers through fluorescence turn-off and turn-on effects (Scheme 1). The sensing mechanisms were explored in detail, and relevant insights for practical applications were provided.

2. Experimental

2.1. Materials and general measurements

All chemicals and solvents used for the experiments were purchased from Shanghai Aladdin Biochemical Technology Co., Ltd, which are above analytical reagent grade. Mass percentage content (w%): $MnSO_4\cdot 4H_2O$ (≥99.9 %), ligands (≥98 %), chloride salts (≥99.9 %), potassium salts (≥99.5 %), food additives (≥99 %), sweat biomarkers (≥99 %). Fourier transform infrared (FTIR) spectrum was recorded on a Bruker VERTEX 80 spectrometer using a powdered sample on a KBr disk in the 4000-400 cm^{-1} region for identifying the coordination interaction between the ligand and metal center. After the heat treatment, elemental analysis was carried out on a Perkin Elmer 2400LS elemental analyzer for determining the elemental composition (C, H and N) of the sample. Thermogravimetric analysis (TGA) was investigated on an SDT Q600 instrument, which was carried out at a heating rate of 10 °C·min^{-1} in nitrogen atmosphere for evaluating the thermal stability of the sample. Powder X-ray diffraction (PXRD) patterns were collected on an X'pert Philips diffractometer using a Cu-K_α radiation source ($\lambda = 1.5418$ Å) for confirming the crystallinity and phase purity of the samples. Luminescence excitation and emission spectra were recorded on a Perkin Elmer LS55 fluorescence spectrophotometer at room temperature for evaluating luminescent performance of the samples. Ultraviolet–visible (UV–Vis) absorption spectra were collected on an Agilent Cary 60 spectrophotometer for analyzing the absorption behavior of the samples. X-ray photoelectron spectroscopy (XPS) measurement was performed on a Thermo Scientific ESCALAB 250Xi photoelectron spectrometer for providing elemental composition and analyzing surface interactions of the samples with analytes. The density-functional theory (DFT) was employed to perform self-consistent calculations through the PWSCF module for obtaining the HOMO-LUMO orbital energy levels of H_2L and organic analytes.

2.2. Synthesis of MOF-*1*

A mixture of $MnSO_4\cdot 4H_2O$ (0.022 g, 0.1 mmol), 4,4′-bipy (0.016 g, 0.1 mmol) and H_2L (0.0116 g, 0.05 mmol) dissolved in H_2O (15 mL) was heated to 130 °C and maintained at this temperature for 2 days in a 20 mL Teflon-lined stainless steel, and then cooled to room temperature.

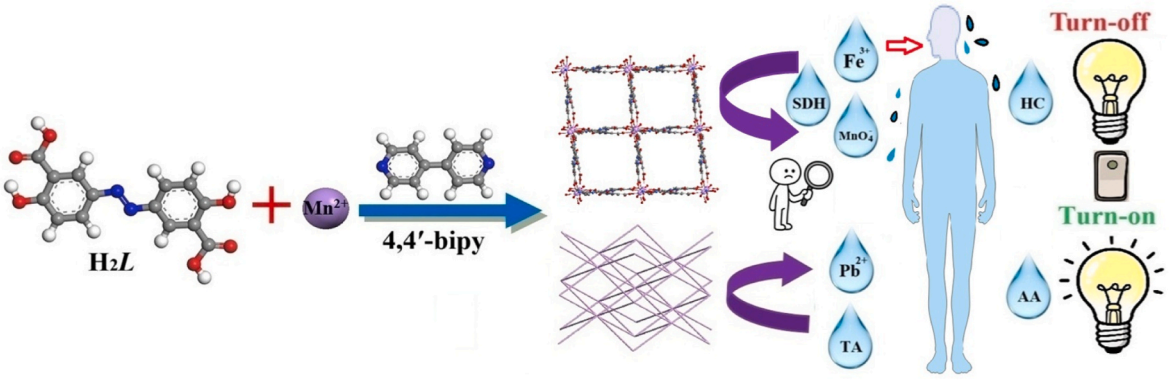

Scheme 1. Schematic representation of the construction of MOF-**1** for selective detection.

Yellow blocked crystals were collected by filtration and washing with ethanol in a yield of 76 % based on H_2L. Anal. Calc. for $C_{96}H_{80}Mn_4N_{16}O_{32}$ (2189.52) C, 52.66; H, 2.39; N, 10.24 (%). Found: C, 52.67; H, 2.42; N, 10.26 (%). FTIR (KBr, cm^{-1}): 3038m, 1638s, 1575s, 1479s, 1442s, 1346s, 1252s, 1181m, 1067w, 928w, 836m, 803m, 677m, 620m, 585m, 481m.

2.3. Fluorescence measurements

Sensing experiments. MOF-**1** suspensions were prepared by separately dispersing 3 mg of MOF-**1** powder in 3 mL of deionized water and various aqueous solutions of analytes (0.01 mol·L^{-1}). The mixtures were ultrasonicated for 15 min to form homogeneous suspensions, and their fluorescence spectra were recorded under the optimal excitation wavelength (λ_{ex} = 365 nm) of MOF-**1** at room temperature.

Fluorescence titration experiments. 3 mg of MOF-**1** powder was dispersed in deionized water (3 mL) and ultrasonicated for 15 min to form a homogeneous suspension. The suspension was subsequently transferred to a 1 cm-width quartz cell, and its fluorescence responses were record (λ_{ex} = 365 nm) with the dropwise addition of the analyte solution (3×10^{-4}, 3×10^{-3}, 3×10^{-2} and 3×10^{-1} mol·L^{-1}).

Competition experiments. MOF-**1** suspensions were prepared by separately dispersing 3 mg of MOF-**1** powder in 3 mL of different solutions. These solutions included: (1) the solutions of each coexisting substance (0.01 mol·L^{-1}); (2) mixed solutions of the analyte (0.01 mol·L^{-1}) and each coexisting substance (0.01 mol·L^{-1}) at a molar ratio of 1:1. The mixtures were ultrasonicated for 15 min to form homogeneous suspensions, the fluorescence spectra of all suspensions were recorded (λ_{ex} = 365 nm). The maximum fluorescence intensities were compared to evaluate the interference of each coexisting substance on the fluorescence change of MOF-**1** to the analyte.

Recyclable experiments. After the first fluorescence sensing experiment, 3 mg of MOF-**1** powder was centrifugated and washed with deionized water for several times to remove residual analyte. The recovered MOF-**1** powder was collected, dried at 60 °C for 2 h to remove residual water. The treated MOF-**1** powder was subsequently used in the successive fluorescence experiments to evaluate its recycling stability.

Spike and recovery experiments. Three real water samples, including tap water (from Fushun), spring water (Nongfu Spring), and river water (Hunhe River) were collected, and a real sweat sample was collected from a healthy adult volunteer following the standard sweat sampling protocol. All samples were pretreated via centrifugation to remove insoluble impurities. Different solutions of target analytes were separately spiked into the pretreated samples. 3 mg of MOF-**1** powder was dispersed in each 3 mL spiked sample and ultrasonicated for 15 min to form a homogeneous suspension, and the analytes were then determined by fluorescence spectroscopy.

2.4. X-ray crystallographic measurement

The crystallographic data for MOF-**1** were collected by the φ-ω scan technique on a Bruker D8 VENTURE diffractometer equipped with graphite monochromated Mo-K_α radiation (λ = 0.71073 Å) at 193 K. The structure was solved by direct method using SHELXS package [24], and refined by the full-matrix least-squares using SHELXTL package [25]. All non-hydrogen atoms were refined anisotropically, whereas the hydrogen atoms fixed to their geometrically ideal positions were treated by a mixture of independent and constrained refinement. The coordinated 4,4'-bipy molecules (N5, N6, N9 and N10) are disordered. The atomic occupancy rates of Mn2, O15, O16, O17 and O18 are all 0.5. The detailed crystallographic data of MOF-**1** are summarized in Table 1, and selected bond lengths and angles are listed in Table 2. The cif file contains the crystallographic data, which has been deposited in the Cambridge Crystallographic Data Center (CCDC 2452562).

Table 1
Crystal and refinement data for MOF-**1**.

Chemical formula	$C_{96}H_{80}Mn_4N_{16}O_{32}$
M_r	2189.52
Crystal system, space group	Monoclinic, *C*2/*c*
Temperature (K)	193
a, *b*, *c* (Å)	28.1279(8), 19.5310(5), 18.4966(5)
α, β, γ (°)	90, 113.190(1), 90
V (Å^3)	9340.4(4)
Z	4
Radiation type	Mo-K_α
μ (mm^{-1})	0.63
Crystal size (mm)	0.12 × 0.1 × 0.1
T_{min}, T_{max}	0.672, 0.746
No. of measured, independent and observed [$I > 2\sigma(I)$] reflections	43970, 10686, 6939
R_{int}	0.081
$(\sin\theta/\lambda)_{max}$ (Å^{-1})	0.65
$R[F^2 > 2\sigma(F^2)]$, $wR(F^2)$, *S*	0.062, 0.168, 1.04
No. of reflections	10686
No. of parameters	895
No. of restraints	321
R_1, wR_2 [$I \geq 2\sigma(I)$]	0.0620, 0.1406
R_1, wR_2 (all data)	0.1081, 0.1679
$\Delta\rho_{max}$, $\Delta\rho_{min}$ (e·Å^{-3})	1.98, −0.75

Table 2
Selected bond lengths and bond angles for MOF-**1**.

Mn2–O13^{i}	2.234(2)	Mn1–O13^{i}	2.334(2)
Mn2–O13	2.234(2)	Mn1–O1	2.161(2)
Mn2–O8	2.176(2)	Mn1–O4^{iv}	2.139(3)
Mn2–O8^{i}	2.176(2)	Mn1–O7	2.115(3)
Mn2–O11^{ii}	2.167(2)	Mn1–O10^{ii}	2.119(3)
Mn2–O11^{iii}	2.167(2)	Mn1–N5	2.276(3)
O13–Mn2–O13^{i}	178.18(13)	O1–Mn1–O13^{i}	89.63(9)
O8–Mn2–O13	88.68(9)	O1–Mn1–N5	93.54(10)
O8–Mn2–O13^{i}	92.67(9)	O4^{iv}—Mn1—O13^{i}	87.15(9)
O8^{i}—Mn2—O13^{i}	88.68(9)	O4^{iv}—Mn1—O1	93.39(10)
O8^{i}—Mn2—O13	92.67(9)	O4^{iv}—Mn1—N5	82.12(11)
O8–Mn2–O8^{i}	84.19(14)	O7–Mn1–O13^{i}	90.11(9)
O11^{iii}—Mn2—O13	91.39(9)	O7–Mn1–O1	90.03(10)
O11^{iii}—Mn2—O13^{i}	87.27(9)	O7–Mn1–O4^{iv}	175.60(10)
O11^{ii}—Mn2—O13^{i}	91.38(9)	O7–Mn1–O10^{ii}	86.67(11)
O11^{ii}—Mn2—O13	87.27(9)	O7–Mn1–N5	100.44(11)
O11^{iii}—Mn2—O8	179.62(11)	O10^{ii}—Mn1—O13^{i}	90.44(9)
O11^{iii}—Mn2—O8^{i}	95.43(10)	O10^{ii}—Mn1—O1	176.71(11)
O11^{ii}—Mn2—O8^{i}	179.62(11)	O10^{ii}—Mn1—O4^{iv}	89.90(11)
O11^{ii}—Mn2—O8	95.43(10)	O10^{ii}—Mn1—N5	87.00(10)
O11^{iii}—Mn2—O11^{ii}	84.95(14)	N5–Mn1–O13^{i}	168.97(10)

Symmetry codes: (i) $-x+1, y, -z+1/2$; (ii) $-x+3/2, y-1/2, -z+1/2$; (iii) $x-1/2, y-1/2, z$; (iv) $-x+3/2, y-1/2, -z+3/2$.

3. Results and discussion

3.1. Crystal structure of MOF-*1*

Single-crystal X-ray diffraction study revealed that MOF-**1** crystallized in the monoclinic system with the space group *C*2/*c* (Table 1). It features a new 3D framework structure. The fundamental unit of MOF-**1** contains a trinuclear Mn cluster, where the Mn centers have two coordination environments, denoted as Mn1 and Mn2 (Fig. 1a). Each Mn1 center is six-coordinated by one N atom from one coordinated 4,4'-bipy molecule, four carboxylate O atoms from four L^{2-} ligands, and one O atom from one coordinated water molecule in an octahedral coordination sphere {$Mn1O_5N$}. Each Mn2 center is hexagonally coordinated by four carboxylate O atoms from four L^{2-} ligands, and two O atoms from two coordinated water molecules in an octahedral coordination sphere {$Mn2O_6$}. Two Mn1 centers and one Mn2 center form a trinuclear Mn cluster with the Mn–Mn distance of 3.799 Å through sharing the O13

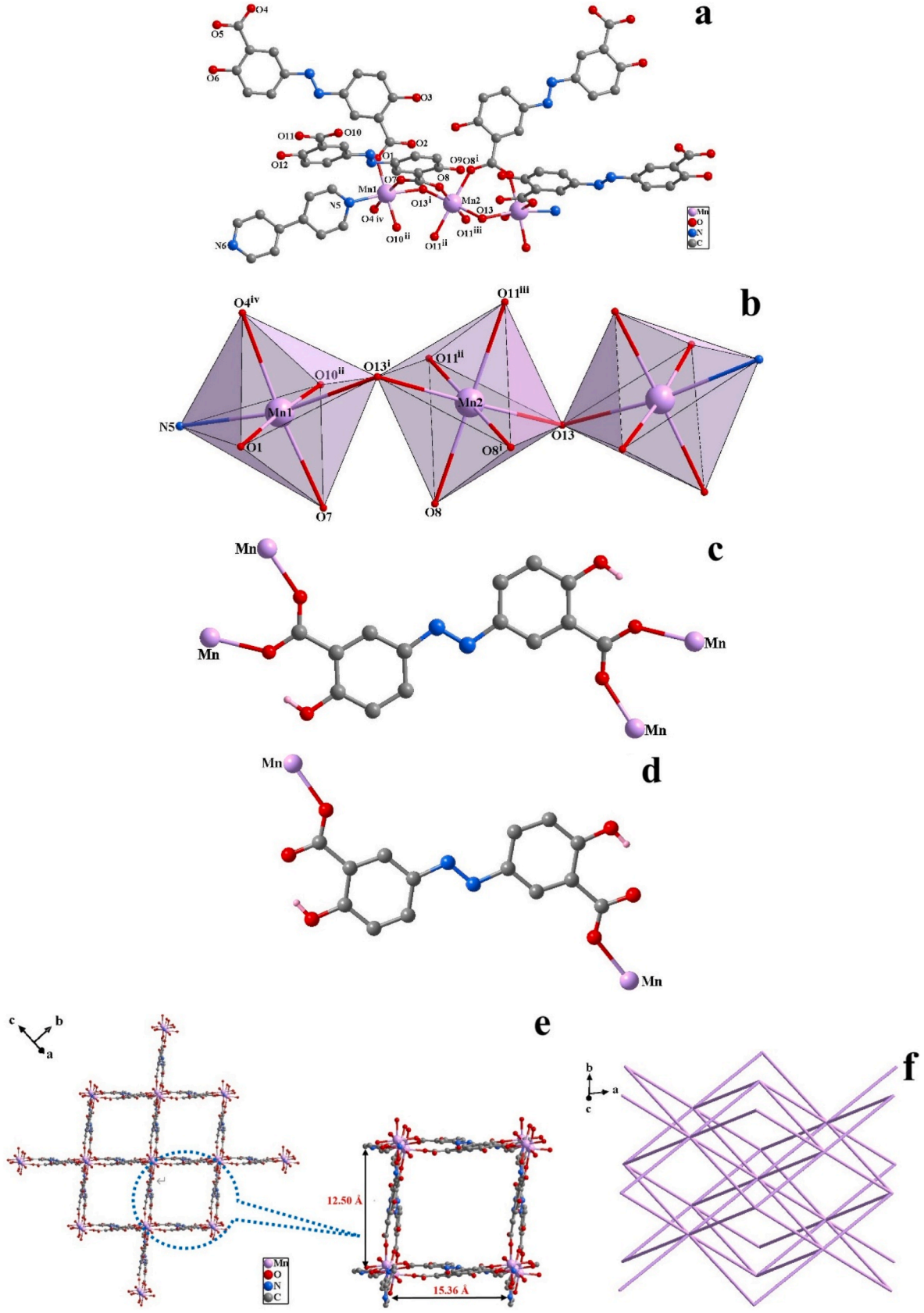

Fig. 1. (a) Coordination environment of Mn centers in MOF-**1**; (b) trinuclear Mn cluster; (c and d) coordination modes of L^{2-} ligands; (e) 3D framework with square channels and (f) topological net of MOF-**1**.

atoms in the μ_2-water molecules (Fig. 1b). The distances of Mn–O are in the range of 2.115(3)-2.334(2) Å, and the length of Mn–N is 2.276(3) Å (Table 2), which are comparable with the bond lengths [26] and angles [27] in previously reported Mn(II)-MOFs. L^{2-} ligands in MOF-**1** link with the trinuclear Mn clusters in two different coordination modes: one links Mn1 and Mn2 centers using its carboxylate groups in uniform bis-bridging mode (Fig. 1c), and the other binds to Mn1 centers adopting its carboxylate groups in uniform bis-monodentate mode (Fig. 1d), whose coordination modes are different from those reported in literature [28]. These isolated adjacent trinuclear Mn clusters are connected together by L^{2-} ligands to construct a new 3D framework with 1D square channels with 12.50 Å × 15.36 Å (Fig. 1e). The introduced 4,4'-bipy ligand only serves as a terminal molecule and is not involved in the construction of this 3D framework.

To get a better understanding the complicated framework of MOF-**1**, the topological method was employed to analyze the structure by TOPOSPRO [29]. The trinuclear Mn cluster can be considered as an eight-connected node surrounded by eight L^{2-} ligands, and each L^{2-} ligand acts as a bridge to link two trinuclear Mn clusters through its carboxylate groups, and the intricate framework of MOF-**1** can thus be simplified into an eight-connected net with the point symbol of $\{4^{12}\cdot6^8\}$ (Fig. 1f) [30].

3.2. PXRD and TGA

The experimental PXRD pattern of MOF-**1** matched well with those simulated from single-crystal diffraction data (Fig. S1), demonstrating the high phase purity of the synthesized product.

To determine the stability of MOF-**1**, its thermal behavior was studied in the temperature range of 25–600 °C with a heating rate of 10 °C·min^{-1} in nitrogen atmosphere (Fig. S2). It experienced three steps of weight loss. The first weight loss of 6.5 % between 25 and 130 °C corresponds to the removal of coordinated and free water molecules (Calcd: 6.6 %). The second weight loss of 28.9 % between 130 and 360 °C is assigned to the decomposition of the coordinated 4,4'-bipy molecules (Calcd: 28.5 %). The third weight loss between 360 and 600 °C is due to the framework collapse accompanied by the decomposition of L^{2-} ligands. The final residue is MnO (Calcd:13.0; Found: 13.4 %).

3.3. Luminescence property

Considering the outstanding photoluminescence of MOFs and their potential in chemical sensors, the luminescence properties of free H_2L precursor and MOF-**1** were explored in the solid state at room temperature. The free H_2L precursor exhibited intense broad emission band at 393 nm, and MOF-**1** at 389 nm (λ_{ex} = 292 nm) (Fig. 2a). The emission of H_2L precursor may be attributed to the intraligand π*→π or π*→n transitions [31], and the emission of MOF-**1** can be ascribed to the intraligand charge transition owing to the similarity in the shape of the fluorescence emission of MOF-**1** with H_2L precursor. The calculated CIE coordinates can be obtained as (0.157, 0.190), which is located in the blue region (Fig. 2b). The observed weakened emission band of MOF-**1** with respect to H_2L precursor suggested the involvement of charge transfer transition between L^{2-} ligands and metal centers.

3.4. Chemical stability

The chemical stability of MOF-based fluorescence probes is of crucial significance for sensing specific analytes. It is not only directly related to the detection performances, but also to their application in complicated real-world environments, particularly in acidic and alkaline solutions. The stability of MOF-**1** was evaluated by immersing samples in pH 1–14 aqueous solutions for 24 h, and the PXRD patterns of MOF-**1** treated with pH 2–13 solutions showed negligible change compared to the simulated one from the single-crystal diffraction data (Fig. 3). This result demonstrates that MOF-**1** can remain intact in water, and even in acidic and alkaline solutions for at least 24 h.

3.5. Detection of metal ions

Iron ion (Fe^{3+}) and lead ion (Pb^{2+}) are two harmful pollutants for human health. Excessive intake of iron can cause gastrointestinal mucosa damage, liver and pancreas damage, liver fibrosis and cirrhosis, while lead pollution can lead to serious abdominal pain, diarrhea, neurological damage and renal dysfunction.

Considering the excellent chemical stability and fluorescence performance of MOF-**1**, the fluorescence responses of MOF-**1** to various metal ions in water were investigated. The powder samples of MOF-**1** were dispersed in 0.01 mol·L^{-1} of various MCl_x (M^{x+} = Pb^{2+}, Ba^{2+}, Cd^{2+}, Zn^{2+}, Ni^{2+}, Mn^{2+}, Co^{2+}, Cr^{3+}, Cu^{2+}, Na^{+}, K^{+}, Mg^{2+}, Ca^{2+}, Al^{3+}, Sr^{2+}, and Fe^{3+}) aqueous solutions. The suspension containing only MOF-**1** was used as a fluorescent blank to evaluate the responses to different cations. The metal ions caused a different degree of fluorescence turn-off or turn-on effect (Fig. 4a). Fe^{3+} induced a significant quenching in the fluorescence intensity of MOF-**1** with a quenching efficiency of 97 %, and Pb^{2+} induced a remarkable 3.8-fold enhancement (Fig. 4b). These results indicate that MOF-**1** presents the potential for detection of Fe^{3+} and Pb^{2+} in aqueous media.

To explore the sensing performance of MOF-**1** towards trace Fe^{3+} and

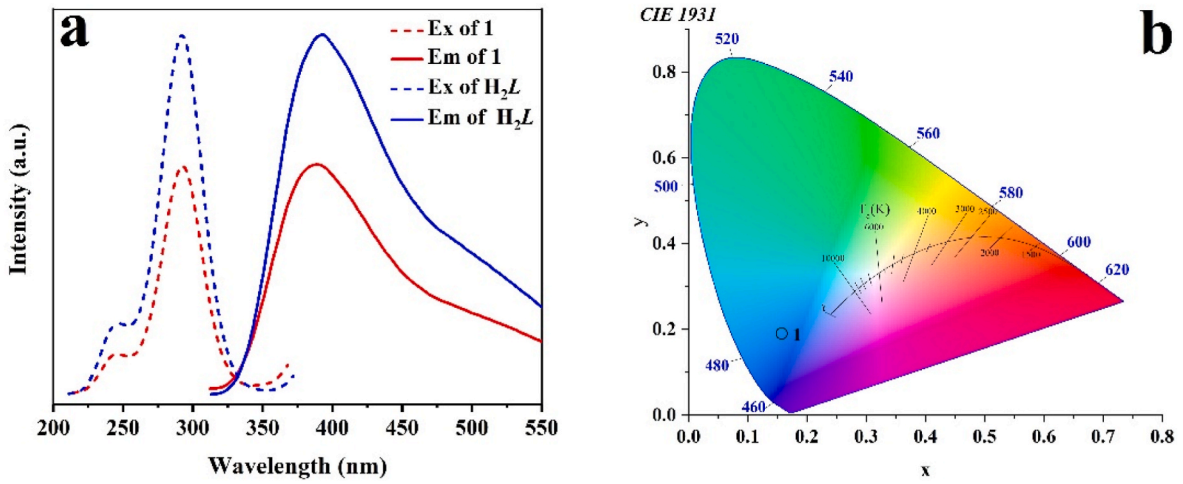

Fig. 2. (a) Excitation and emission spectra of MOF-**1** and H_2L precursor in the solid-state at room temperature; (b) CIE chromaticity diagram of MOF-**1**.

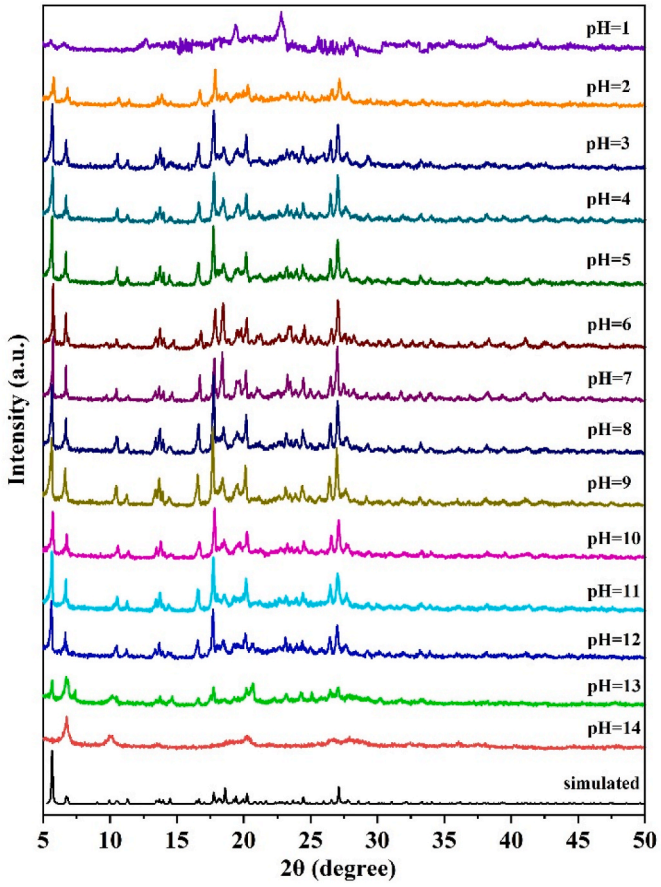

Fig. 3. PXRD patterns for MOF-**1** under different pH conditions.

Pb^{2+} in water, corresponding titration experiments were performed. The fluorescence intensity of MOF-**1** was gradually reduced with dropwise addition of Fe^{3+} solution (Fig. 5a), and it was progressively enhanced with dropwise addition of Pb^{2+} solution (Fig. 5c). The quenching and enhancement efficiencies can be fitted by the Stern-Volmer equation of $I_0/I = 1 + K_{sv}[M]$, where I_0 and I are the fluorescence intensities in the absence and presence of the analyte, K_{sv} is the slope, representing the Stern-Volmer constant, and [M] refers to the molar concentration of the analyte. The result revealed a good linear relationship between I_0/I ratio and Fe^{3+}/Pb^{2+} molar concentration with corresponding R^2 values of 0.998 (Figs. 5b) and 0.997 (Fig. 5d). The corresponding K_{sv} values were found to be 1.17×10^5 and 2.63×10^4 M^{-1}, and the limits of detection (LODs) can be calculated to be 3.85×10^{-7} and 1.71×10^{-6} M with the formula of $3\delta/K_{SV}$ (δ refers to the standard deviation of ten blank measurements) [32]. The LOD values of MOF-**1** are comparable to those of the previously reported MOF-based sensors (Table 3) [33–42], while it exhibits sensitive dual-signal responses towards Fe^{3+} and Pb^{2+}.

The competitive experiments were carried out to evaluate the anti-interference ability of MOF-**1** to detect Fe^{3+} and Pb^{2+}. MOF-**1** can still detect Fe^{3+} and Pb^{2+} in the presence of coexisting ions (Fig. 6a and b). The results suggest that MOF-**1** has high selectivity towards Fe^{3+} and Pb^{2+}.

The cyclic experiments were performed to evaluate the recoverability of MOF-**1** as a chemical sensor. The initial luminescence intensity of MOF-**1** can be almost completely recovered by centrifugation and washing with deionized water after sensing Fe^{3+} or Pb^{2+} (Fig. 7a and b). These results demonstrate that MOF-**1** exhibits good recyclability for the detection of Fe^{3+} and Pb^{2+}.

Some experiments and measurements were carried out to study the possible mechanism for the detection of Fe^{3+} with MOF-**1**. The PXRD pattern of MOF-**1** treated by Fe^{3+} solution was consistent with the simulated one from single-crystal diffraction data (Fig. 8a), indicating that the framework of MOF-**1** remained intact [43]. This result excluded the possibility that the fluorescence quenching of MOF-**1** by Fe^{3+} was caused by framework collapse. When Fe^{3+} was added to the suspension of MOF-**1**, the exchange interaction of the Fe^{3+} ions with Mn centers was difficult to complete due to the disparities of electronic structures, valence state and coordination ability. The cationic replacement that causes the fluorescence quenching can also be ruled out. The UV–Vis absorption spectrum of Fe^{3+} was measured. Its absorption spectrum effectively overlapped with the excitation and emission bands of MOF-**1** (Fig. 8b), which suggested that the fluorescence quenching of MOF-**1** by Fe^{3+} is caused by the competitive absorption (CA) of excitation light between MOF-**1** and Fe^{3+}, and resonance energy transfer (RET) from MOF-**1** to Fe^{3+}. A comparative analysis with relevant literature highlights the uniqueness of the sensing mechanism of MOF-**1** for Fe^{3+}. Li et al. [21] reported two Cd-based CPs using biphenyldicarboxylate derivative (1,1′-biphenyl-2,3,3′,5′-tetracarboxylic acid) as the ligand, which also exhibit selective fluorescence quenching for Fe^{3+}. Their proposed mechanism is that the quenching effect is primarily attributed to the RET process. The discrepancy arises from differences in the spectral overlap characteristic between MOF-**1** and the Cd-based CPs. In Li et al.′s work, the absorption spectrum of Fe^{3+} likely overlapped only with the emission bands of the Cd-based CPs, eliminating the CA pathway. Di et al. [44] reported a Zn(II)-MOF synthesized using 3,3′,5,5′-azobenzenetetracarboxylate ($abtc^{4-}$) ligand. The absorption spectrum of Fe^{3+} likely overlapped with the excitation band of the Zn(II)-MOF,

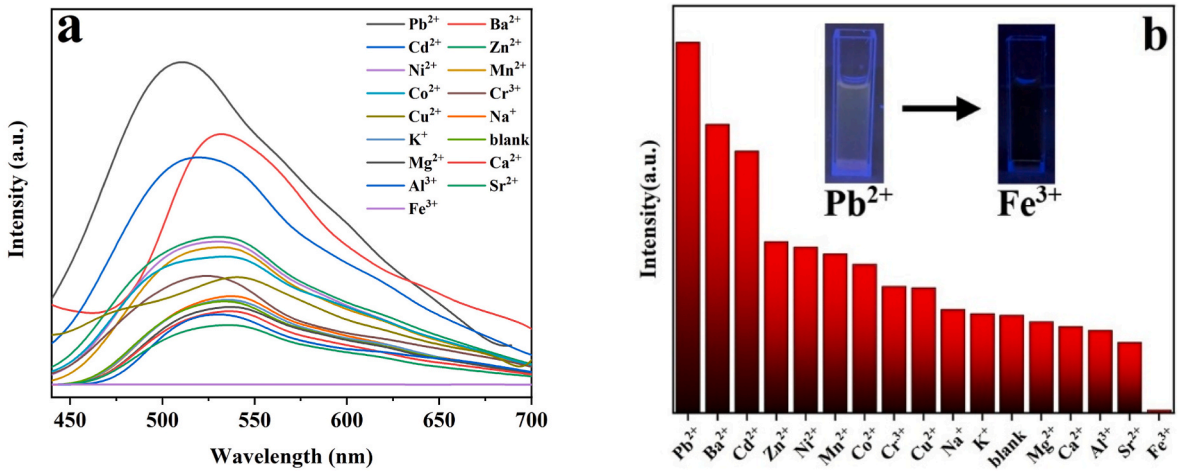

Fig. 4. (a) Fluorescence responses of MOF-**1** to different metal ions; (b) different luminescence intensities of MOF-**1** in the presence of different metal ions.

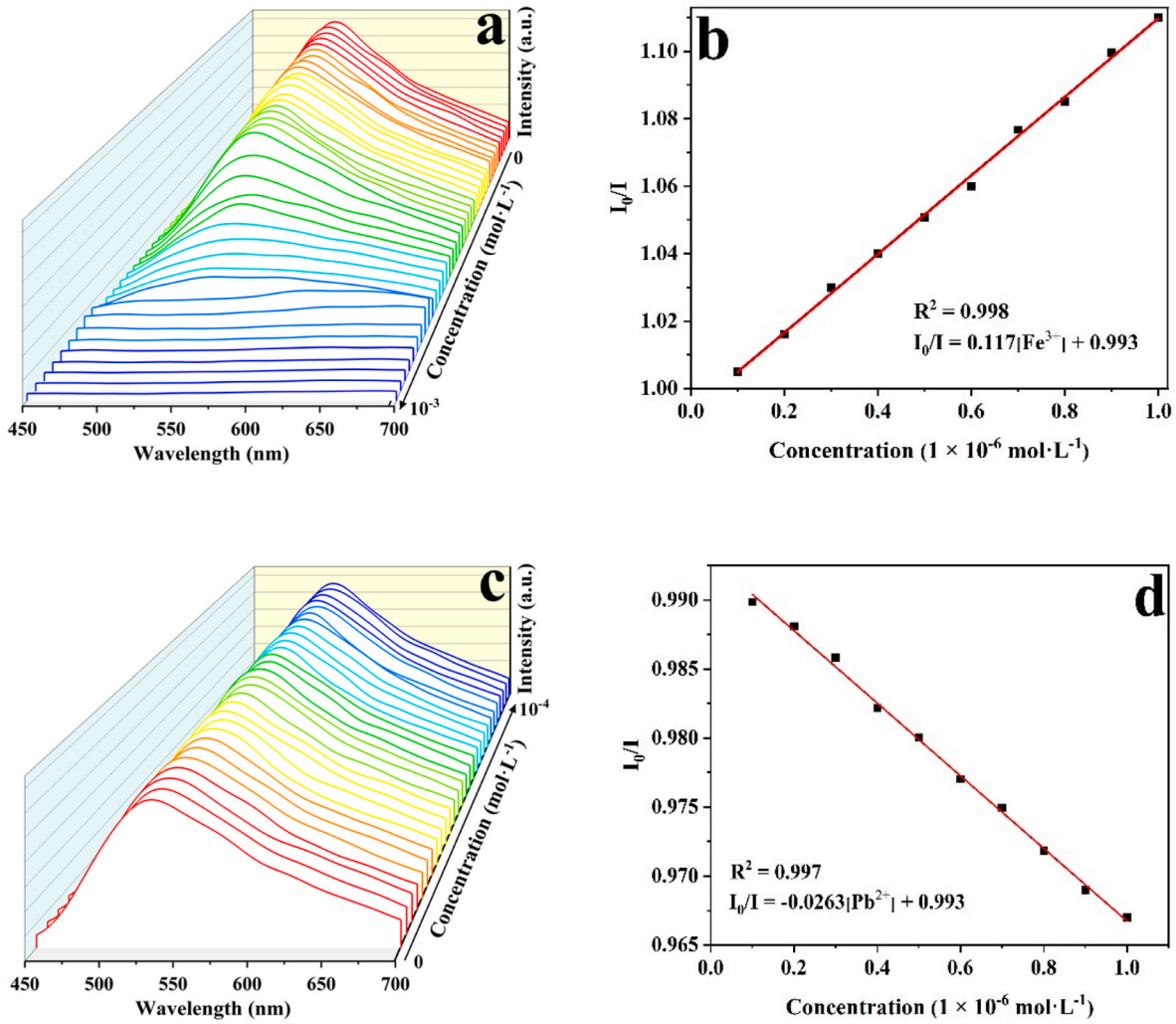

Fig. 5. (a and c) Fluorescence responses of MOF-**1** to different amounts of Fe^{3+} and Pb^{2+}; (b and d) Stern-Volmer plots of MOF-**1** with gradually increasing amounts of Fe^{3+} and Pb^{2+}.

Table 3
Comparison of MOF-based sensors for the detection of Fe^{3+} and Pb^{2+}.

Sensor	Analyte	Analytical signal	K_{sv}/M^{-1}	LOD/M	Reference
MOF-**1**	Fe^{3+}	Turn-off	2.47×10^4	1.82×10^{-6}	This work
$[Zn(pbba)(H_2O)]\cdot 3dmf\cdot 2H_2O$	Fe^{3+}	Turn-off	1.2×10^4	4.5×10^{-6}	[33]
$[Tb_2(\mu_3\text{-}L)_2(\mu_4\text{-}L)(H_2O)_3]_n\cdot nH_2O$	Fe^{3+}	Turn-off	6.85×10^5	4.81×10^{-8}	[34]
$[Tb(tftba)_{1.5}(phen)(H_2O)]_n$	Fe^{3+}	Turn-off	4.043×10^4	1.27×10^{-5}	[35]
$\{[Cd(dbtdb)(1,2,4\text{-}H_3btc)]\cdot 0.5H_2O\}_n$	Fe^{3+}	Turn-off	3.3×10^3	1.1×10^{-3}	[36]
$[Zn_2(bpt)(OH)(L)]\bullet 2H_2O$	Fe^{3+}	Turn-off	3.45×10^4	7.39×10^{-6}	[37]
MOF-**1**	Pb^{2+}	Turn-on	2.63×10^4	1.71×10^{-6}	This work
$[Zn(tdc)(tmb)]_n$	Pb^{2+}	Turn-off	4.91×10^5	1.78×10^{-6}	[38]
$[Tb(ppda)(npdc)_{0.5}(H_2O)_2]_n$	Pb^{2+}	Turn-on	1.05×10^5	9.44×10^{-5}	[39]
$Ag(bpy)(ipaNH_2)$	Pb^{2+}	Turn-off	2×10^4	2.1×10^{-6}	[40]
$[Cd_3(L)_2(bpy)]_n$	Pb^{2+}	Turn-off	1.29×10^4	1.43×10^{-6}	[41]
$[Eu_2(fdc)_3(dma)(H_2O)_3]\cdot dma\cdot 4.5H_2O$	Pb^{2+}	Turn-on	2.97×10^6	8.22×10^{-6}	[42]

and this phenomenon was attributed to the CA process between $abtc^{4-}$ ligand and Fe^{3+}. The RET process is not a contributing factor to the fluorescence quenching of the Zn(II)-MOF toward Fe^{3+}.

To investigate additional factors contributing to the fluorescence quenching in MOF-**1**, XPS measurements on pristine MOF-**1** and those treated by Fe^{3+} solution were carried out (Fig. 8c). The O1s peak in the MOF-**1** treated by Fe^{3+} shifted by 0.3 eV compared with the pristine MOF-**1** (Fig. 8d), whereas the N1s peak remained unchanged (Fig. 8e). It indicates that the uncoordinated Lewis basic sites of carboxylate groups in MOF-**1** have weak interactions with Fe^{3+}, which can affect the efficient energy transfer from L^{2-} ligands to Mn centers, thereby inducing fluorescence quenching of MOF-**1**.

The mechanism of fluorescence response towards Pb^{2+} was demonstrated. The crystal structure of MOF-**1** treated with Pb^{2+} solution remained intact (Fig. 9a), indicating that the possibility that fluorescence enhancement was caused by framework collapse can be ruled out. Upon adding Pb^{2+} to the suspension of MOF-**1**, the fluorescence emission was immediately enhanced, suggesting that the possibility of

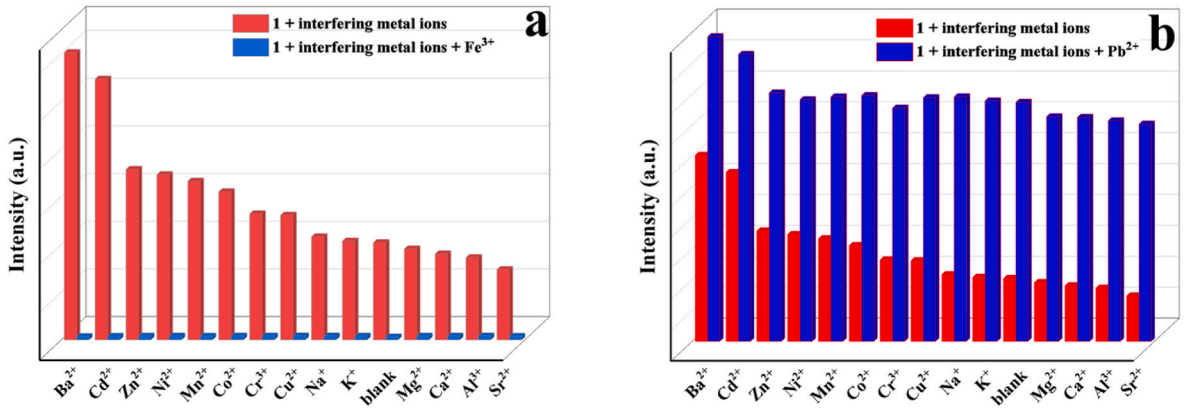

Fig. 6. Anti-interference test of MOF-**1** in water for detection of (a) Fe^{3+} and (b) Pb^{2+}.

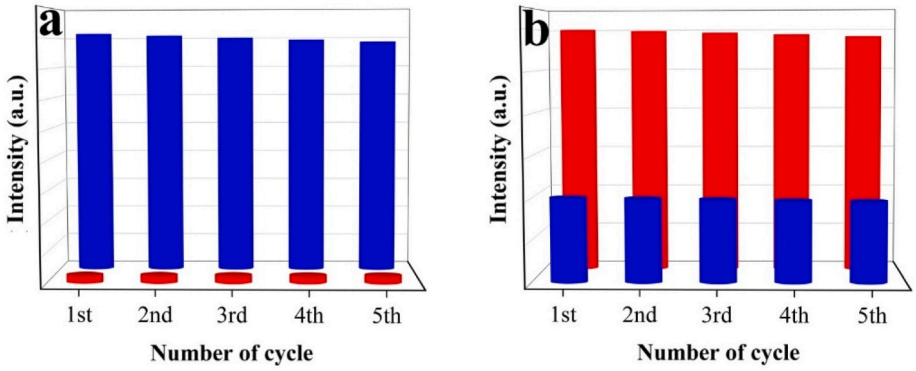

Fig. 7. Recycling tests of MOF-**1** in water for detection of (a) Fe^{3+} and (b) Pb^{2+}.

cationic replacement was also ruled out. The XPS spectrum of MOF-**1** treated by Pb^{2+} solution was measured (Fig. 9b). The C1s peak shifted from 281.8 to 282 eV compared with the pristine MOF-**1** (Fig. 9c), while the O1s and N1s peaks remained unchanged (Fig. S3), which may result from the weak interactions of Pb^{2+} with the benzene moieties in L^{2-} ligands [45]. Such interactions may affect the singlet and triplet excited states of L^{2-} ligands and increase the ligand-centered energy transfer efficiency, and thus cause the luminescent enhancement of MOF-**1** [46]. The absorption band of Pb^{2+} showed no overlap with the excitation and emission bands of MOF-**1** (Fig. 9d), indicating that the mechanism was unrelated to conventional quenching factors like the CA and RET processes.

3.6. Detection of inorganic anions

The fluorescence intensities of MOF-**1** dispersed in 0.01 mol·L^{-1} of different K_nX (X^{n-} = Cl^-, $H_2PO_4^-$, Br^-, NO_3^-, SO_4^{2-}, F^-, $Cr_2O_7^{2-}$, CO_3^{2-}, PO_4^{3-} and MnO_4^-) solutions were detected (Fig. 10a). MOF-**1** demonstrated an obvious fluorescence quenching effect towards MnO_4^- with the quenching efficiency of 97 % (Fig. 10b). The result of a fluorescence titration experiment indicated that the fluorescence intensity of MOF-**1** was gradually reduced with dropwise addition of MnO_4^- solution (Fig. 10c). The linear relationship between the intensity ratio and the concentration of MnO_4^- was fitted by using the equation of $I_0/I = 1 + K_{sv}[M]$ with R^2 value of 0.995 (Fig. 10d). The K_{sv} value was found to be 1.954×10^5 M^{-1}, and the LOD value was calculated to be 2.303×10^{-7} M through the formula of $3\delta/K_{SV}$. The two values are comparable to those of the previously reported luminescent sensors for the detection of MnO_4^- (Table 4) [47–51], indicating highly sensitive sensing capacity of MOF-**1** towards MnO_4^-. When various anionic aqueous solutions were introduced into the suspension of MOF-**1** with additional MnO_4^-, MOF-**1** can still detect MnO_4^- (Fig. 10e). The result of regeneration experiments showed that the fluorescence quenching and recovery of MOF-**1** were basically unchanged in five runs (Fig. 10f), indicating the good reusability of MOF-**1** for fluorescence detection.

The possible mechanism for the detection of MnO_4^- with MOF-**1** was investigated. The framework of MOF-**1** remained intact after soaking in MnO_4^- solution (Fig. 11a). This result ruled out the possibility that fluorescence quenching of MOF-**1** by MnO_4^- was caused by framework collapse. The FTIR spectrum of MOF-**1** treated with MnO_4^- solution was consistent with that of pristine MOF-**1** (Fig. S4), indicating that the possibility of anion exchange causing the fluorescence quenching was ruled out. The absorption band of MnO_4^- covered part of the excitation and emission spectra of MOF-**1** (Fig. 11b), indicating that the fluorescence quenching was caused by the CA of excited energy between MOF-**1** and MnO_4^-, and the RET from MOF-**1** to MnO_4^- [51]. This mechanism is different from the turn-on effect for sensing MnO_4^- reported in recent literature [52].

3.7. Detection of food additives

The same procedure was implemented to explore the sensing performance of MOF-**1** towards food additives by using the solutions of tartaric acid (TA), $NaNO_2$, quinoline yellow (QY), methylparaben (MPB), aspartame (APM), butylated hydroxytoluene (BHT), propyl gallate (PG), tert-butylhydroquinone (TBHQ), and dehydroacetic acid sodium salt (SDH) (Fig. 12a). The results indicate that SDH can induce complete quenching to the luminescence intensity of MOF-**1**, and TA can cause a remarkable enhancement (Fig. 12b). The corresponding fluorescence titration experiments showed that the fluorescence intensity of MOF-**1** was gradually reduced with the dropwise addition of SDH solution (Fig. 12c), and it was gradually enhanced with the dropwise

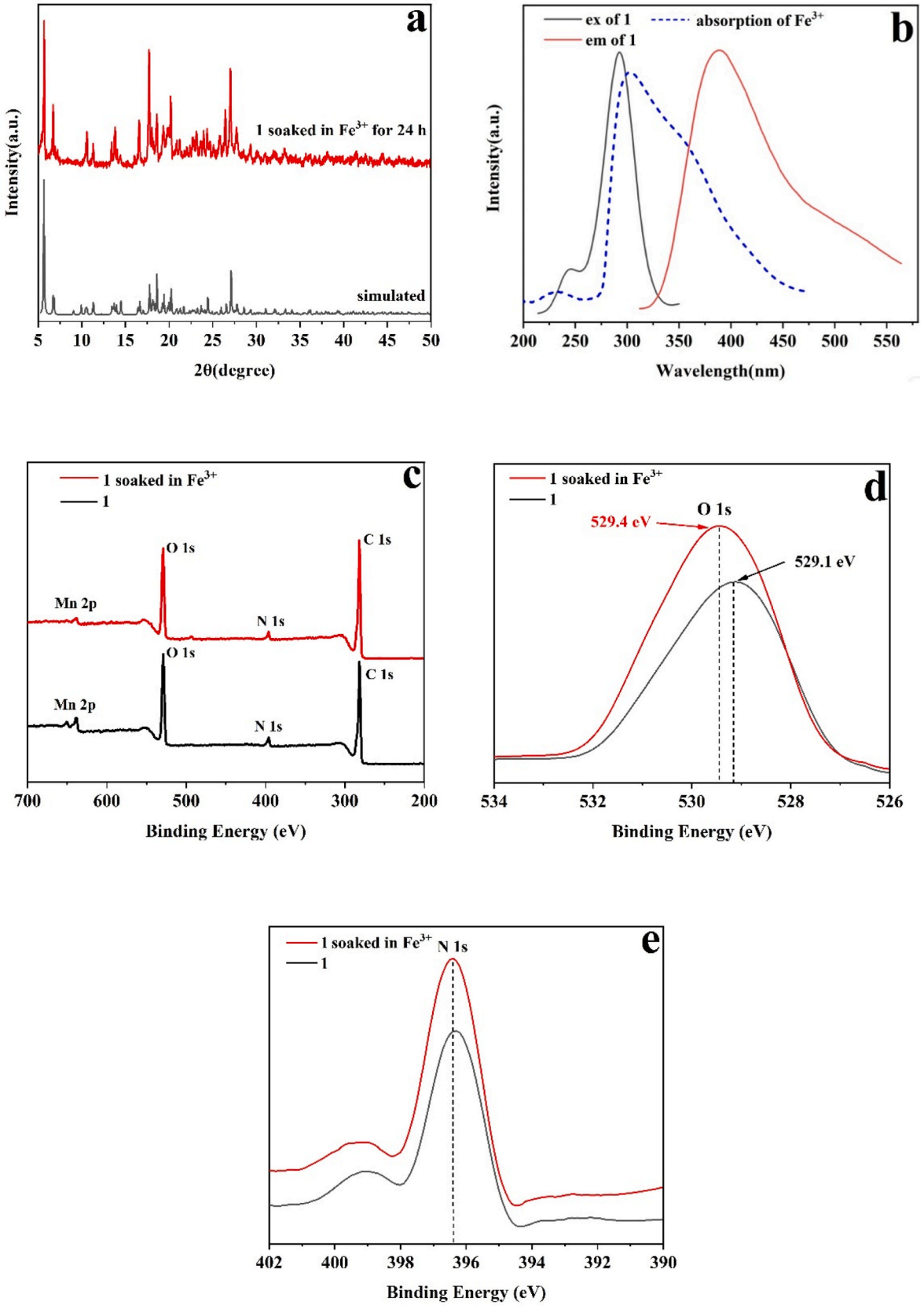

Fig. 8. (a) Experimental PXRD pattern of MOF-**1** treated by Fe^{3+} solution and simulated PXRD pattern of MOF-**1** from single-crystal diffraction data; (b) UV–Vis absorption of Fe^{3+}, excitation and emission spectra of MOF-**1**; (c) XPS spectra of pristine MOF-**1** and those treated by Fe^{3+} solution; (d) O 1s; and (e) N 1s.

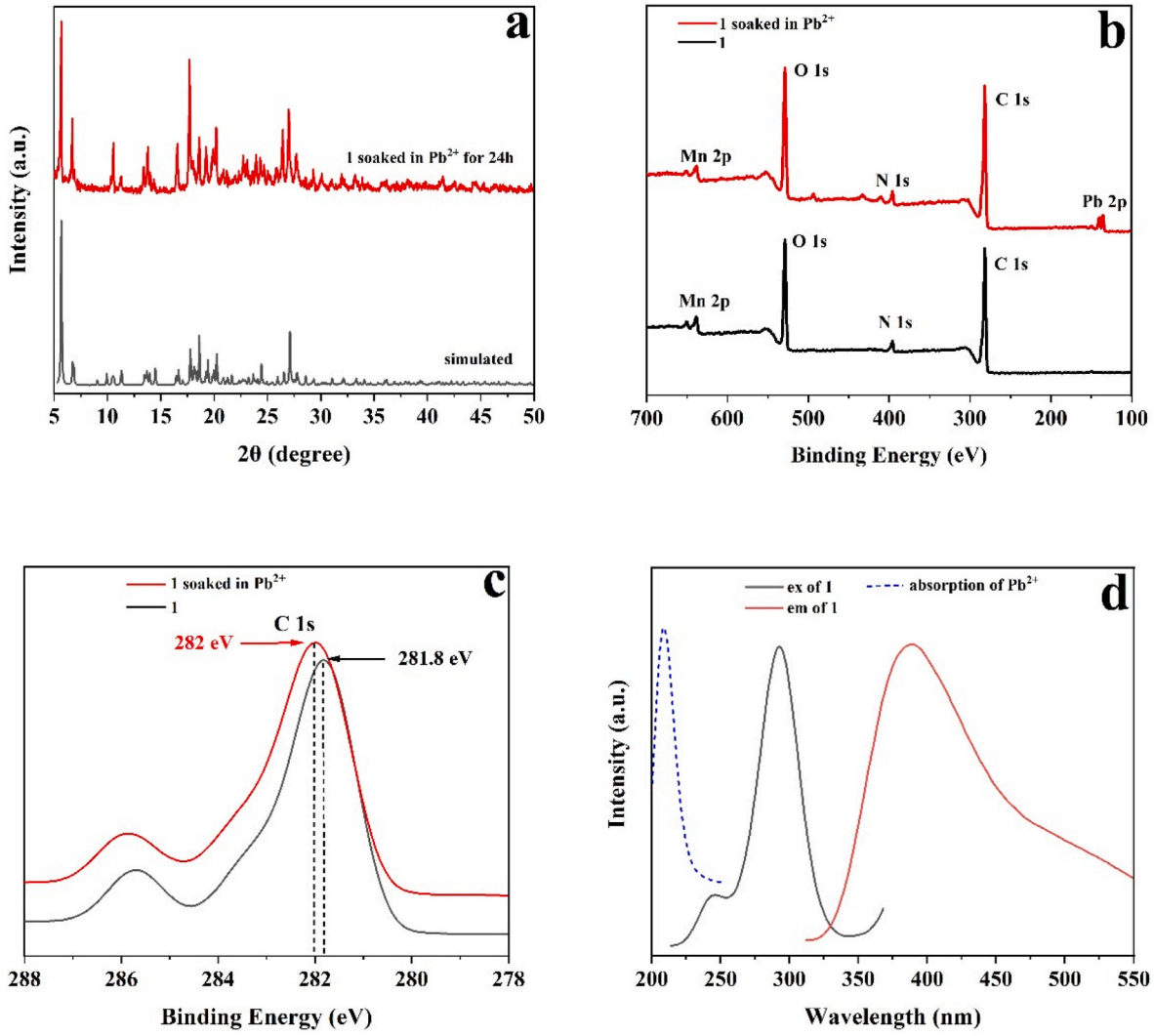

Fig. 9. (a) Experimental PXRD pattern of MOF-**1** treated by Pb^{2+} solution and simulated PXRD pattern of MOF-**1** from single-crystal diffraction data; (b) XPS spectra of pristine MOF-**1** and those treated by Pb^{2+} solution; and (c) C 1s; (d) UV–Vis absorption of Pb^{2+}, excitation and emission spectra of MOF-**1**.

addition of TA addition (Fig. 12e). The quenching and enhancement processes of the luminescence of MOF-**1** with respect to the SDH and TA concentrations can be fitted by Stern–Volmer equation of $I_0/I = 1 + K_{sv}[M]$ with corresponding R^2 values of 0.999 (Figs. 12d) and 0.998 (Fig. 12f). The corresponding K_{sv} values were determined to be 7.746×10^5 and $1.32 \times 10^5\ M^{-1}$, and the LODs were calculated to be 5.81×10^{-8} and 3.41×10^{-7} M by utilizing the formula of $3\delta/K_{sv}$. While the detection of food additives, such as melamine, curcumin, sodium salicylate and lysine, have been extensively reported in the field of food safety, whose LOD values can reach the 0.1 μM level [53–55], there is still a lack of detailed research on the dual-signal detection of SDH and TA. The LOD values obtained in this work are comparable to those previously reported about other food additives [53–55]. When SDH or TA was introduced into a suspension of MOF-**1** with coexisting food additive in competitive experiments, the fluorescence intensity was remarkably quenched or enhanced, indicating that MOF-**1** can selectively detect SDH and TA (Fig. 12g and h). The results of recycling experiments showed that the fluorescence detection and recovery capabilities of MOF-**1** remained almost unchanged in five runs (Fig. 12i and j), indicating MOF-**1** is a reusable fluorescent probe for detection of SDH and TA.

Some experiments and measurements were carried out to study the possible mechanisms for sensing SDH and TA with MOF-**1**. The PXRD patterns of MOF-**1** samples were measured after separate treatment with SDH and TA solutions to confirm the structural maintenance, thereby ruling out the possibility that the fluorescence changes were caused by structural collapse. (Fig. 13a). The FTIR spectrum of MOF-**1** treated with SDH or TA solution was consistent with that of pristine MOF-**1** (Fig. S5), thereby indicating that the fluorescence changes were not caused by the anionic replacement. The UV–Vis absorption spectrum of SDH solution showed moderate overlap with the excitation spectrum of MOF-**1**, but no overlap with the emission spectrum, illustrating that the luminescent quenching of MOF-**1** was induced by the CA mechanism [56]. The UV–Vis absorption spectrum of TA solution showed no overlap with the excitation and emission spectra of MOF-**1** (Fig. 13b). This result provides indirect evidence for the fluorescence enhancement of MOF-**1** in the presence of TA due to the absence of fluorescence quenching factors like CA and RET processes. To explore the effects of other factors on fluorescence changes, density functional theory (DFT) calculations were carried out to determine the energy levels of the lowest unoccupied molecular orbital (LUMO) and highest occupied molecular orbital (HOMO) of H_2L, SDH and TA (Fig. 13c). The HOMO energy level (−6.044 eV) of H_2L is lower than that of SDH (−5.031 eV), which indicates that the photoinduced electron transfer (PET) process involves electron transfer from the HOMO of SDH to the valence band of H_2L, and thus causes fluorescence quenching. The LUMO value (−2.145 eV) of TA is much higher in energy than that of H_2L (−2.489 eV), thus the electrons within the LUMO of TA would populate the conduction band of

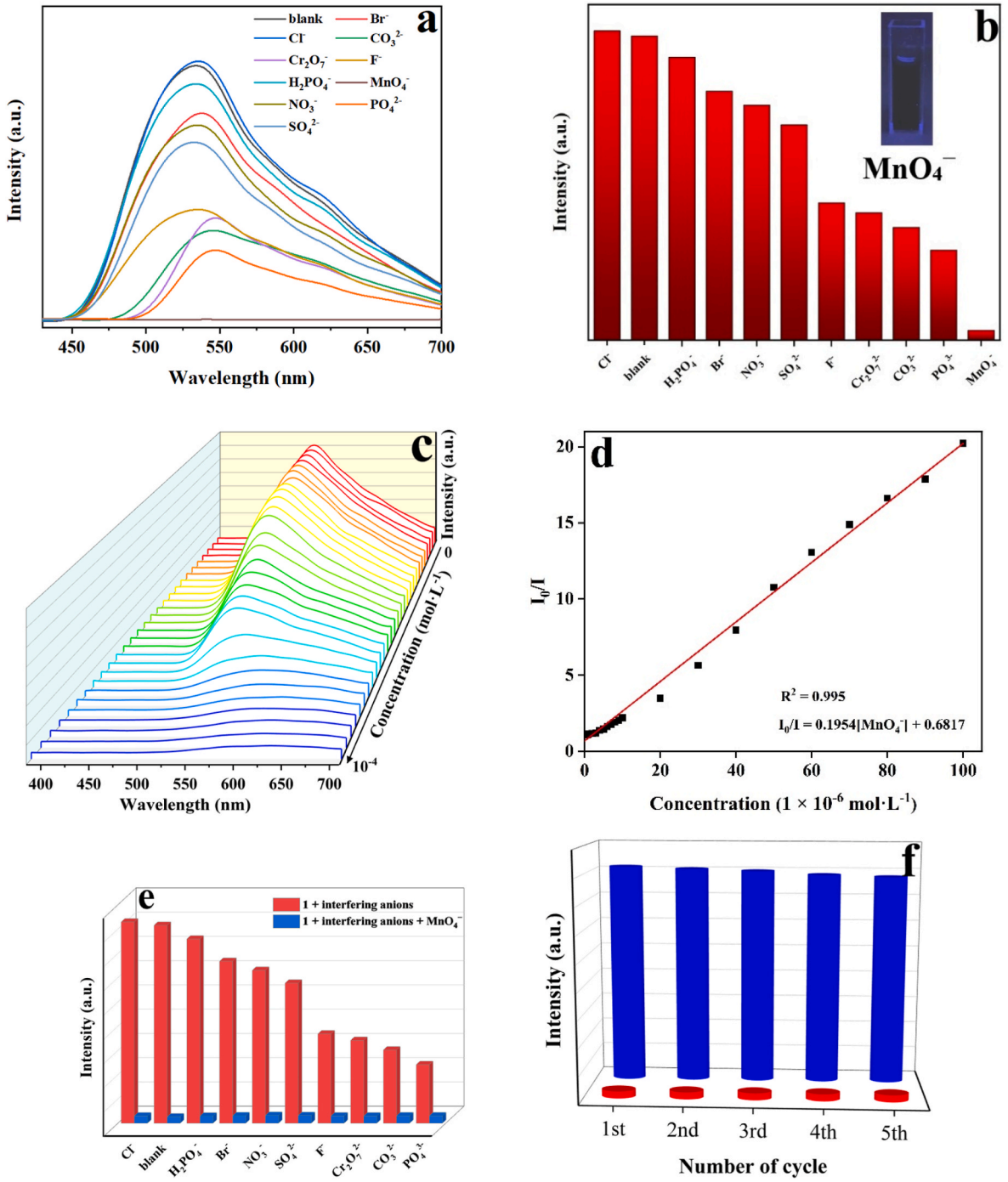

Fig. 10. (a) Fluorescence responses of MOF-**1** to different inorganic anions; (b) different luminescence intensities of MOF-**1** in the presence of different inorganic anions; (c) fluorescence responses of MOF-**1** to different amounts of MnO_4^-; (d) Stern-Volmer plot of MOF-**1** with gradually increasing amount of MnO_4^-; (e) anti-interference test and (f) recycling test of MOF-**1** in water for detection of MnO_4^-.

Table 4
Comparison of MOF-based sensors for the detection of MnO_4^-.

Sensor	Analyte	Analytical signal	K_{sv}/M^{-1}	LOD/M	Reference
MOF-**1**	MnO_4^-	Turn-off	1.954×10^5	2.303×10^{-7}	This work
$(H_2bpp)\cdot[(UO_2)^{2+}(nip)_3]\cdot H_2O$	MnO_4^-	Turn-off	1.88×10^4	1.79×10^{-6}	[47]
$[Tb(btta)_{1.5}(H_2O)_{4.5}]_n$	MnO_4^-	Turn-off	8.88×10^5	3.90×10^{-7}	[48]
$\{[Ag(L)]BF_4\cdot H_2O\}_n$	MnO_4^-	Turn-off	2.77×10^5	1.81×10^{-6}	[49]
$[Tb_2(L)_2(H_2O)_2\cdot 5H_2O\cdot 6dmac]_n$	MnO_4^-	Turn-off	1.2×10^3	4.48×10^{-8}	[50]
$[Zn(L)_2]\cdot 2dmf$	MnO_4^-	Turn-off	1.92×10^4	2.34×10^{-5}	[51]

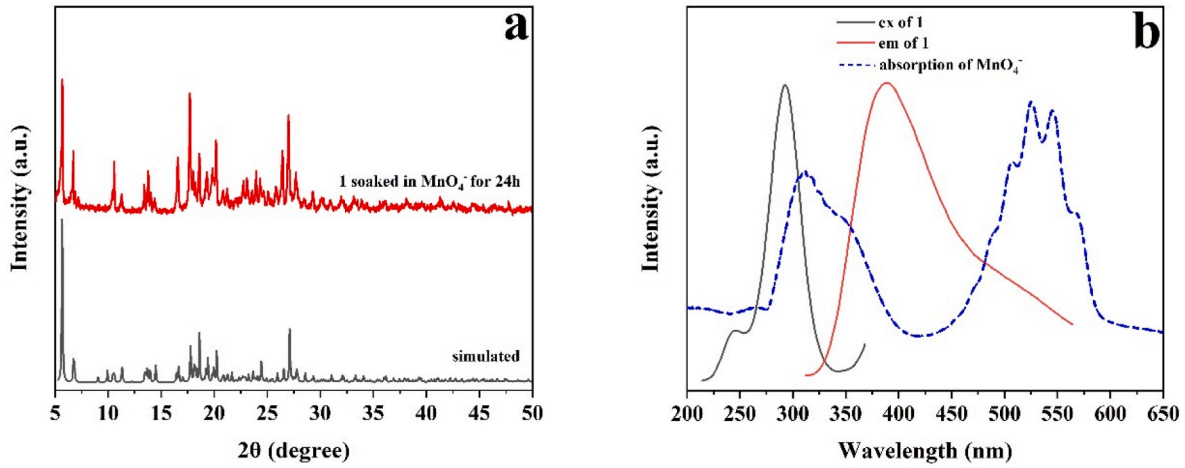

Fig. 11. (a) Experimental PXRD pattern of MOF-**1** treated with MnO_4^- solution and simulated PXRD pattern of MOF-**1** from single-crystal diffraction data; (b) UV–Vis absorption of MnO_4^-, excitation and emission spectra of MOF-**1**.

H_2L upon photoexcitation of TA [57]. This electron transfer mechanism effectively enhances the fluorescence intensity of the H_2L system [58]. The fluorescence changes of MOF-**1** towards SDH and TA are thus all assigned to the PET processes.

3.8. Detection of sweat biomarkers

Biomarkers in body fluids can reflect the interactions between a biological system and external chemical factors by indicating the adverse effects of water pollutants and food additives. Significant progress has been made in the development and application of fluorescence-based detection of biomarkers in tear [59], saliva [59], urine [60] and serum [60], while the research on sweat-based biomarker detection remains relatively underexplored. The advantages of sweat-based biomarker detection include easy accessibility and non-invasiveness to the human body. Excessive intake of water pollutants and food additives by the human body can damage cellular structures and organ functions, which in turn leads to abnormal changes in the contents of sweat biomarkers. Detecting these biomarkers is vital for effectively preventing the health damage caused by these substances.

MOF-**1** has laid a foundation for further investigation into its fluorescence selective sensing toward sweat biomarkers owing to its excellent acid-base stability in a broad pH range and good water stability [61]. Human sweat can be defined as aqueous solutions containing various chemicals like urea (Ure), ascorbic acid (AA), glutamic acid (Glu), methionine (Met), glucose (Glc), hydrocortisone (HC), alanine (Ala), uric acid (UA), glycine (Gly), creatinine (Cre), and proline (Pro). MOF-**1**-based fluorescent probe was used for the detection of the above-mentioned chemicals. The MOF-**1** samples were separately dispersed in the solutions of individual sweat chemicals. HC caused a drastic quenching in the emission of MOF-**1** with a quenching efficiency of 95 %, and AA caused a 3.4-fold enhancement in emission intensity (Fig. 14a and b). The result indicates that MOF-**1** can act as a promising dual-signal fluorescence sensor for the detection of HC and AA.

To explore the sensing performance of MOF-**1** towards trace HC and AA in water, corresponding titration experiments were performed. The fluorescence responses of MOF-**1** suspension varied with different concentrations of HC and AA. The maximum emission intensity was gradually reduced with increasing HC concentration (Fig. 14c), while it was enhanced with increasing AA concentration (Fig. 14e). The nearly linear relationship between the fluorescence intensity ratio and the concentration of HC or AA was fitted by the Stern–Volmer equation of $I_0/I = 1 + K_{sv}[M]$ with corresponding R^2 values of 0.999 (Figs. 14d) and 0.995 (Fig. 14f). The K_{sv} values are found to be 1.87×10^5 and 2.47×10^4 M^{-1}. The LODs for HC and AA were calculated to be 2.41×10^{-7} and 1.82×10^{-6} M by the formula of $3\delta/K_{SV}$. The detection of AA using MOF-based fluorescent probes has become relatively common, while the dual-signal detection of HC and AA in sweat using MOF-based probes remains scarce. The LOD values obtained in this work are comparable to those reported in previous studies on AA detection (Table 5) [58,62–65].

To investigate the selective detection ability of MOF-**1**, corresponding competitive experiments were performed. The results showed that the detection of HC and AA was not affected by coexisting sweat biomarkers (Fig. 14g and h). The regeneration experiments were performed to explore the reusability of MOF-**1**. The fluorescence detection and recovery capabilities of MOF-**1** remained almost unchanged in five runs (Fig. 14i and j). The results indicate that MOF-**1** has good reusability for HC and AA detection.

The mechanisms of MOF-**1** in the detection of HC and AA were investigated. The PXRD patterns of MOF-**1** samples treated by HC and AA solutions were consistent with the simulated pattern from single-crystal diffraction data, indicating that MOF-**1** samples still maintained framework integrity (Fig. 15a). The possibility that the luminescence changes were caused by the structural collapse of MOF-**1** can be excluded. The positions of the absorption peaks in the FTIR spectra of MOF-**1** treated by HC and AA solutions remained unchanged compared with the pristine MOF-**1** (Fig. S6), indicating that the possibility of anion substitution causing fluorescence changes was ruled out. The UV–Vis spectra of these two analytes hardly overlapped with either the excitation spectrum or the emission spectrum of the MOF-**1** (Fig. 15b). The fluorescence quenching induced by HC was not caused by the CA and RET mechanisms. The above-mentioned factors are not the reasons for fluorescence enhancement of MOF-**1** towards AA. Theoretical calculations were carried out to probe deeply into the mechanisms of the fluorescence changes of MOF-**1**, and the energy levels of the HOMO and LUMO for H_2L, HC and AA were thereby obtained (Fig. 13c). The HOMO energy level (−6.044 eV) of H_2L is lower than that of HC (−5.277 eV), which promotes the transfer of electrons from the HOMO of HC to the valence band of H_2L, and leads to fluorescence quenching. The LUMO energy level of AA is −1.668 eV, which is higher than that of H_2L (−2.489 eV). When AA is photoexcited, the electrons in its LUMO would transfer to the conduction band of H_2L, and thus leads to fluorescence enhancement [66]. The results indicate that the PET mechanisms are responsible for the fluorescence changes of MOF-**1** towards HC and AA.

3.9. The application of fluorescence detection

To evaluate the practical application of MOF-**1**-based chemical sensor in real water samples, tap water (from Fushun), spring water (Nongfu Spring), and river water (Hunhe River) were chosen for the

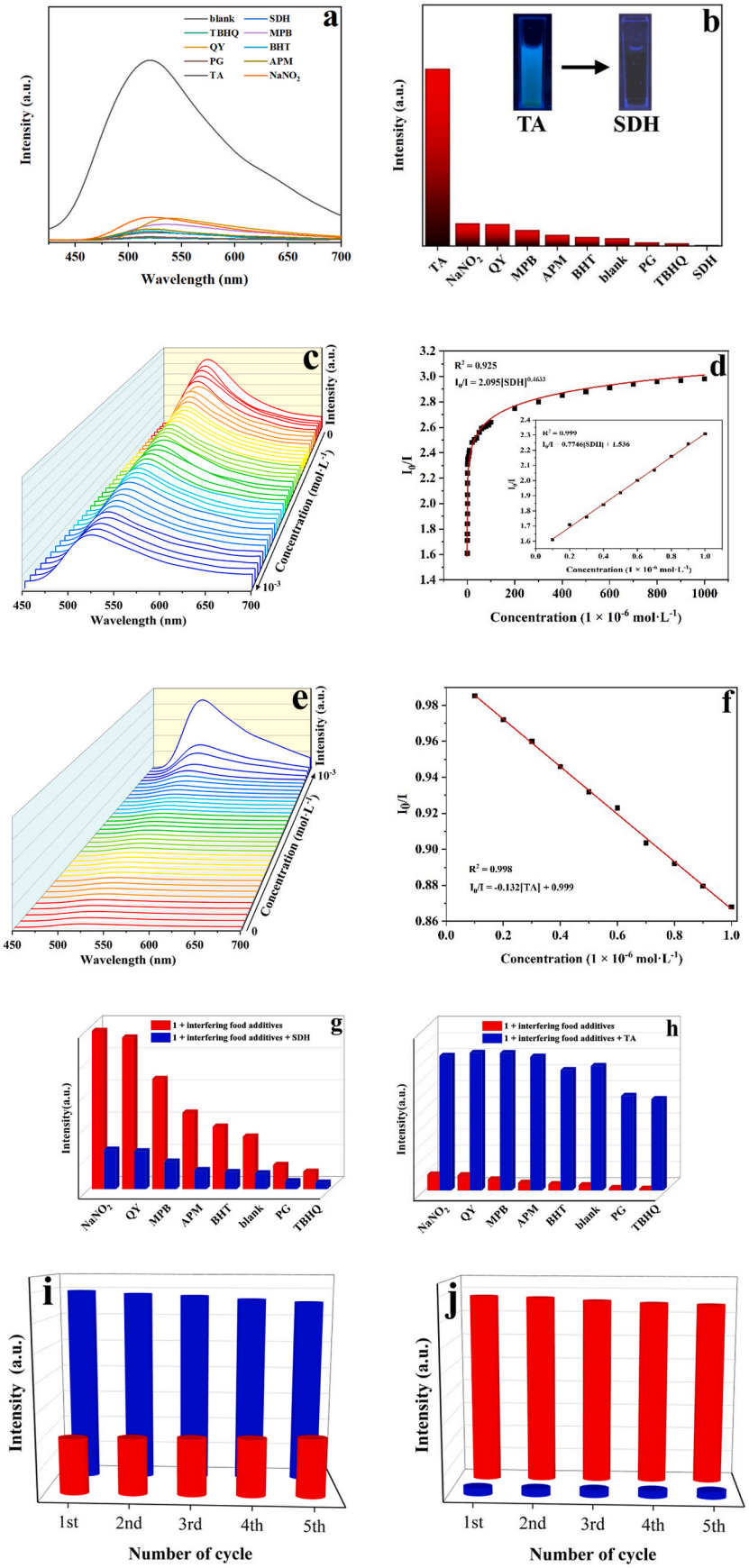

Fig. 12. (a) Fluorescence responses of MOF-**1** to different food additives; (b) different luminescence intensities of MOF-**1** in the presence of different food additives; (c and e) fluorescence responses of MOF-**1** to different amounts of SDH and TA; (d and f) Stern-Volmer plots of MOF-**1** with gradually increasing amounts of SDH and TA; (g and h) anti-interference tests and (i and j) recycling tests of MOF-**1** in water for detection of SDH and TA.

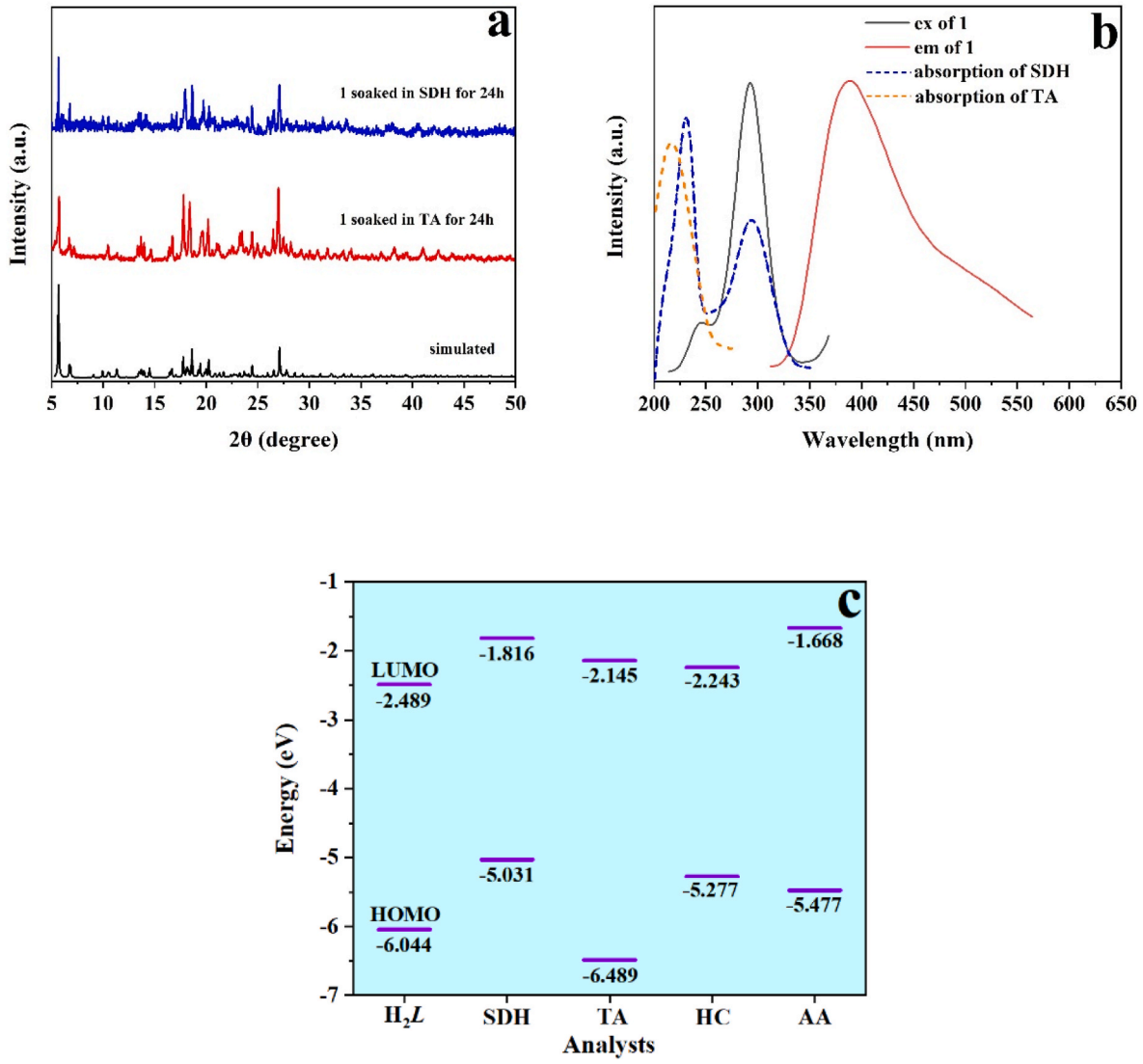

Fig. 13. (a) Experimental PXRD patterns of MOF-**1** samples treated by SDH and TA solutions and simulated PXRD pattern of MOF-**1** from single-crystal diffraction data; (b) UV–Vis absorption of SDH and TA, excitation and emission spectra of MOF-**1**; (c) HOMO and LUMO energy levels for H_2L and the organic analytes.

detection of Fe^{3+}, Pb^{2+} and MnO_4^- using MOF-**1**. The recoveries of Fe^{3+} (98.00%–103.70%), Pb^{2+} (101.10%–102.50%) and MnO_4^- (99.98%–100.40%) were observed, with corresponding relative standard deviations (RSDs) of 0.64%–0.95%, 1.35%–2.12% and 0.03%–0.13% (n = 3) (Table 6). These results suggest that MOF-**1** shows great potential as a sensor for the trace-level detection of Fe^{3+}, Pb^{2+} and MnO_4^- in actual water samples.

To further explore the practical applicability of the MOF-**1**-based chemical sensor in biological fluid, real sweat sample were selected for the detection of HC and AA using MOF-**1**. The HC and AA solutions were separately spiked into the 100-fold diluted sweat samples, and MOF-**1** powder was then employed to determine the target analytes. The experimental results showed that the recoveries of HC and AA were 100.10% and 104.10% with corresponding RSDs of 0.47% and 1.02% (n = 3). (Table 6). The result demonstrates that MOF-**1** sensor can expand its potential application from environmental water samples to biological fluid analysis.

For the purpose of home use, blue-luminescent visible test papers based on MOF-**1** were developed for convenient and fast detection of HC and AA components in the human sweat. The test papers were obtained by immersing filter paper strips in the suspension of MOF-**1** and then drying the strips in an oven at 60 °C (Fig. 16a). Compared with the original test paper under 365 nm UV irradiation (Fig. 16b), the test paper turned bright blue upon exposure to 365 nm UV light after soaking in the AA solution (1×10^{-6} mol·L^{-1}) (Fig. 16c), and it became dark after immersing in the HC solution (1×10^{-6} mol·L^{-1}) (Fig. 16d). MOF-**1** has the potential to serve as a dual-signal rapid-response fluorescent probe, which can be applied to monitor sweat biomarkers for evaluating human health.

4. Conclusions

A new Mn(II)-MOF was successfully synthesized via hydrothermal method with rigid dicarboxylate H_2L precursor. It presents a 3D network structure with 1D square channels built by L^{2-} linkers and trinuclear Mn clusters, featuring a unique $\{4^{12}\cdot6^8\}$ topology. MOF-**1** exhibits excellent chemical stability and emits blue fluorescence. It serves as a reusable dual-signal fluorescent sensor for water pollutants, food additives, and sweat biomarkers in aqueous medium. It not only selectively detects Fe^{3+}, MnO_4^-, SDH and HC in aqueous solution through fluorescence quenching effect, but also recognizes Pb^{2+}, TA and AA via fluorescence enhancement effect. The sensing of Fe^{3+} and MnO_4^- arises from CA and RET mechanisms. Notably, the weak interactions of Fe^{3+} with the uncoordinated carboxylate O atoms also play a role for the fluorescence

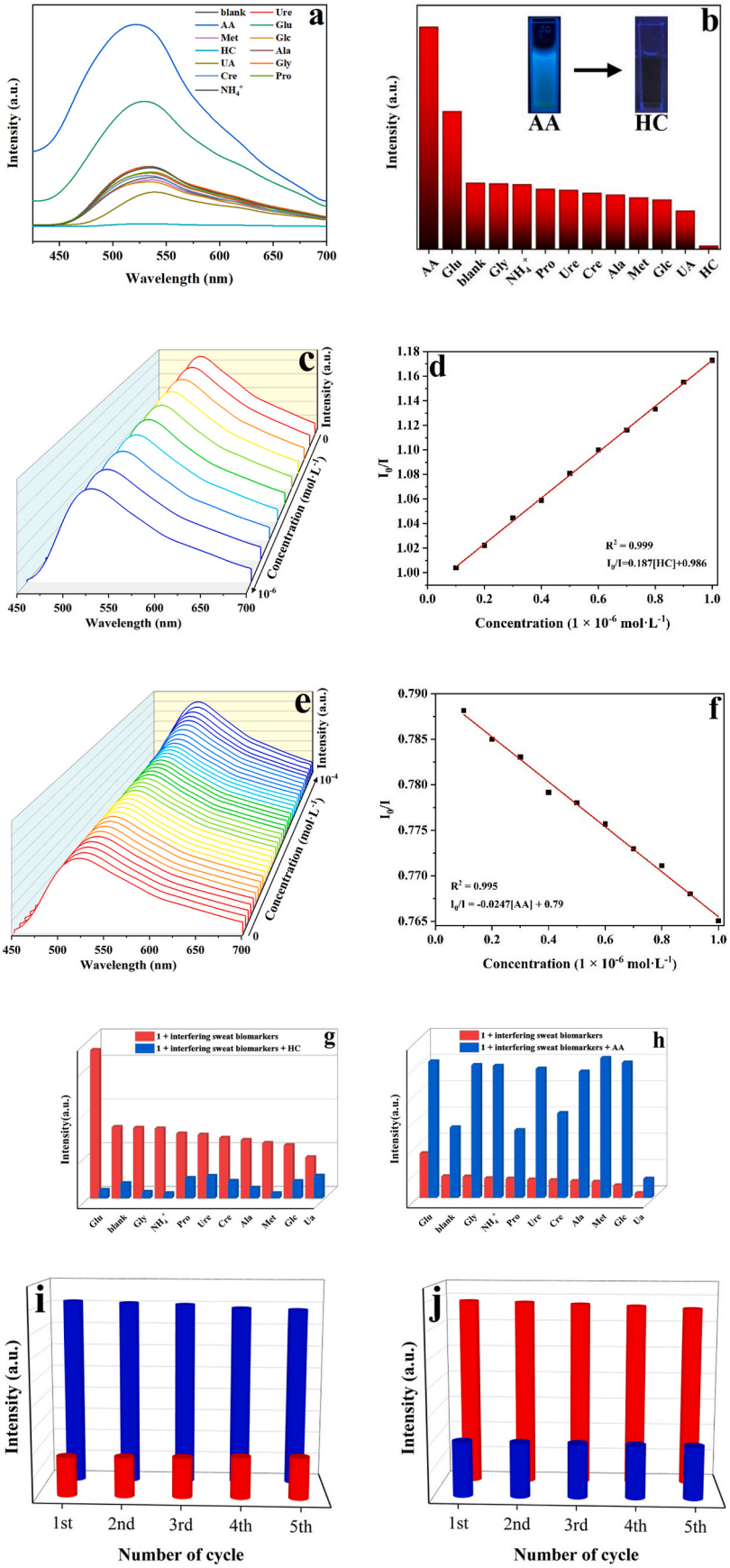

Fig. 14. (a) Fluorescence responses of MOF-**1** to different biomarkers in human sweat; (b) different luminescence intensities of MOF-**1** in the presence of different biomarkers in human sweat; (c and e) fluorescence responses of MOF-**1** to different amounts of HC and AA; (d and f) Stern-Volmer plot of MOF-**1** with gradually increasing amounts of HC and AA; (g and h) anti-interference tests and (i and j) recycling tests of MOF-**1** in water for detection of HC and AA.

Table 5
Comparison of MOF-based sensors for the detection of AA.

Sensor	Analyte	Analytical signal	K_{sv}/M^{-1}	LOD/M	Reference
MOF-**1**	AA	Turn-on	2.47×10^4	1.82×10^{-6}	This work
$[Ni(HL)(bpe)_{1.5}(H_2O)]$	AA	turn-on	5.17×10^2	3.54×10^{-6}	62
$[Zn(HL)_2(bib)]_n \cdot 0.25H_2O$	AA	Turn-off	4.35×10^2	3.15×10^{-4}	63
$[Tb(Hbtec)(Hntca)(H_2O)_3] \cdot H_2O$	AA	Turn-off	3.54×10^4	8×10^{-5}	58
$[Co(H_2L)_2(bpe)(H_2O)_2]bpe \cdot (H_2O)_4$	AA	Turn-on	3.2×10^2	5.75×10^{-7}	64
[Co(HL)(bpe)]	AA	Turn-on	6.52×10^4	6.8×10^{-5}	65

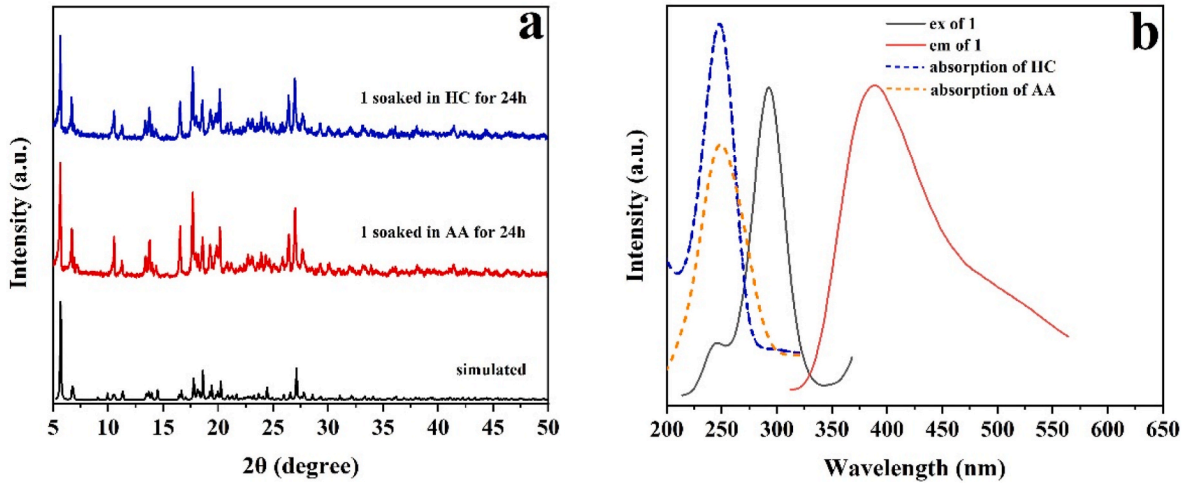

Fig. 15. (a) Experimental PXRD patterns of MOF-**1** samples treated by HC and AA solutions and simulated PXRD pattern of MOF-**1** from single-crystal diffraction data; (b) UV–Vis absorption of HC and AA, excitation and emission spectra of MOF-**1**.

Table 6
Determination of Fe^{3+}, Pb^{2+} and MnO_4^- in real water samples, and HC and AA in real sweat samples.

		Added (μM)	Found (μM)	Recovery (%)	RSD (%, n = 3)
Fe^{3+}	tap water	1.000	0.980	98.00	0.64
	spring water	1.000	1.010	101.00	0.57
	river water	1.000	1.037	103.70	0.95
Pb^{2+}	tap water	1.000	1.013	101.30	1.35
	spring water	1.000	1.011	101.10	2.12
	river water	1.000	1.025	102.50	2.00
MnO_4^-	tap water	10.000	9.998	99.98	0.13
	spring water	10.000	10.040	100.40	0.08
	river water	10.000	10.017	100.20	0.03
HC	1 % sweat	1.000	1.001	100.10	0.47
AA	1 % sweat	1.000	1.041	104.10	1.02

quenching, while the detection of Pb^{2+} is attributed to the weak interactions of Pb^{2+} with the benzene moieties. The PET mechanisms are responsible for the fluorescence changes of MOF-**1** towards TA, HC and AA. The detection of SDH arises from the synergistic effect of the CA and PET mechanisms. The water pollutants in three real-world water samples were detected with recoveries of 98.00–103.70 %, and HC and AA in 100-fold diluted real sweat samples were detected with recoveries of 100.1 % and 104.1 %. MOF-**1**-based test strips were developed for the rapid detection of HC and AA in sweat. This work is one of the few reported examples of detecting sweat biomarkers using MOF-based fluorescent probes. The LOD values of this dual-signal sensor can reach μM level or above. MOF-**1** has the potential to expand the applications of fluorescent MOF in environmental, food, and biological fields, as it can not only detect water pollutants and food additives, but also sense specific sweat biomarkers caused by these substances for assessing health.

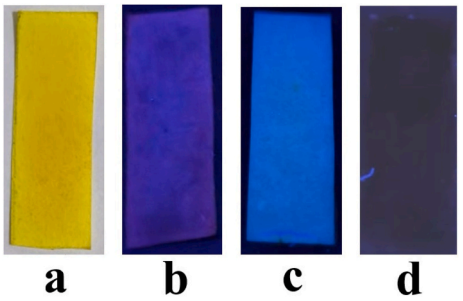

Fig. 16. (a) Photograph of original test paper; (b) under 365 nm UV light, optical images of original test paper and (c and d) those after immersing in AA and HC solutions, respectively.

CRediT authorship contribution statement

Ying Wang: Writing – review & editing, Writing – original draft, Visualization, Validation, Software, Methodology, Investigation, Formal analysis, Data curation, Conceptualization. **Bai-gang An:** Supervision, Resources. **Lei Guan:** Supervision, Resources, Project administration, Investigation, Funding acquisition.

Funding

This research did not receive any specific grant from funding agencies in the public, commercial, or not-for-profit sectors.

Declaration of competing interest

The authors declare that they have no known competing financial interests or personal relationships that could have appeared to influence the work reported in this paper.

Appendix A. Supplementary data

Supplementary data to this article can be found online at https://doi.org/10.1016/j.dyepig.2025.113390.

Nomenclature section

AA	ascorbic acid
Ala	alanine
APM	aspartame
BHT	butylated hydroxytoluene
CA	competitive absorption
CPs	Coordination polymers
Cre	creatinine
DFT	density-functional theory
FTIR	Fourier transform infrared
Glc	glucose
Glu	glutamic acid
Gly	glycine
HC	hydrocortisone
HOMO	highest occupied molecular orbital
I	fluorescence intensity of MOF-**1** when the analyte is present
I_0	fluorescence intensity of MOF-**1**
Ksv	Stern-Volmer constant
LOD	limit of detection
LUMO	lowest unoccupied molecular orbital
Met:	methionine
MOF	metal-organic framework
MPB	methylparaben
PET	photoinduced electron transfer
PG	propyl gallate
Pro	proline
PXRD	powder X-ray diffraction
QY	quinoline yellow
RET	resonance energy transfer
RSD	relative standard deviation
SDH	dehydroacetic acid sodium salt
TA	tartaric acid
TBHQ	tert-butylhydroquinone
TGA	Thermogravimetric analysis
UA	uric acid
Ure	urea
UV–Vis	Ultraviolet–visible
δ	standard deviation

Data availability

Data will be made available on request.

References

[1] Zhang TQ, Zheng FF, Yu TC. Citizens arrest river pollution in China. Nature 2016;535:231.
[2] Wieczorek K, Turek A, Kubicki J, Wolf WM. The long-term effect of industrial waste landfill on surface water. An example from central Poland. Minerals 2021;11:861.
[3] Dasari BM, Aradhi KK, Banothu D, Kurakalva RM. Assessment of groundwater quality, source identification, and health risk around oil and gas drilling sites. Environ Earth Sci 2024;83:312.
[4] Gao WY, Wu KK, Wu C, Chen HR, Li WC, Xue SG. Life cycle assessment of a typical lead smelting process in China. J Clean Prod 2023;415:137796.
[5] Kamyab H, Chelliapan S, Khalili E, Mediavilla DPZ, Khorami M, Aminabhavi TM, et al. Nanobioremediation of heavy metals using microorganisms. J Environ Manag 2025;392:126736.
[6] Bidira F, Al-Senani GM, Bekele EA, Garomsa FS, Vigneshwaran S, Al-Qahtani SD, et al. Synergistic pollutant removal from brewery wastewater using electrocoagulation-assisted pumpkin seed-activated carbon. Process Saf Environ Prot 2025;200:107429.
[7] Shahbazi M, Sabbaghi S, Mirbagheri NS, Saboori R, Mirhosseininia J, Kamyab H, et al. Treatment of metronidazole in wastewater by nano zero-valent iron/copper slag nanocomposite. Sustain Mater Technol 2025;45:e01585.
[8] Ansar SS, Balasubramanian B, Chaudhary A, Pushparaj K, Gopalakrishnan NK, Kamyab H, et al. Microplastics distribution and potential health implications of food and food products. J Food Compos Anal 2025;139:107098.
[9] Wang HT, Bai JY, Miao PY, Wei Y, Chen XC, Lan HB, et al. The key to intestinal health: a review and perspective on food additives. Front Nutr 2024;11:1420358.
[10] Zhang ZL, Li ZH, Wei KC, Cao ZH, Zhu ZG, Chen R. Sweat as a source of non-invasive biomarkers for clinical diagnosis: an overview. Talanta 2024;273:125865.
[11] Saha T, Caño DR, Paz DLE, Sandhu SS, Wang J. Access and management of sweat for non-invasive biomarker monitoring: a comprehensive review. Small 2023;19:2206064.
[12] Qiao YT, Qiao LJ, Chen ZM, Liu BX, Gao L, Zhang L. Wearable sensor for continuous sweat biomarker monitoring. Chemosensors 2022;10:273.
[13] Li YX, Zhang MY, Wang Y, Guan L, Zhao D, Hao XY, et al. A Zn(II) coordination polymer for fluorescent turn-off selective sensing of heavy metal cation and toxic inorganic anions. Molecules 2024;29:2943.
[14] Sadana S, Rajasimman M, Sanjay SK, Kishore V, Rathi BS, Rezania S, et al. Metal–organic framework-enabled biomass conversion technologies for microalgae bio-refinery in the food industry. J Sci Food Agric 2025;105:4680–94.
[15] Guan L, Hao XY, Wang Y, Xiong XJ. A new approach for construction of a SHG–active coordination polymer with multifunctional ligands and Cu ions. J Nonlinear Opt Phys Mater 2025;34:2350067.
[16] Liu XF, Zhang XY, Li RF, Du LY, Feng X, Ding YQ. A highly sensitive and selective "turn off-on" fluorescent sensor based on Sm-MOF for the detection of tertiary butylhydroquinone. Dyes Pigments 2020;178:108347.
[17] Yang HL, Zhang RJ, Zheng TF, Cao C, Peng Y, Chen JL, et al. Aromatic dicarboxylates induced structural diversity of Cd^{II} metal–organic frameworks from a 2D layer to a 3D pillar-layer network for fluorescence sensing of cations, anions and L-serine. Dalton Trans 2025;54:10742–50.
[18] Li DC, Yang YF, Su S, Jia YJ, Xing HW, Hu M. A Eu coordination polymer sensor for the detection of tartrazine, folic acid, and amino acids. Microchem J 2024;199:109995.
[19] Zhao JJ, Zhang L, Liu PY, Chen WZ, Liu ZL, Wang YQ. Water-stable Cd(II)/Zn(II) coordination polymers as recyclable luminescent sensors for detecting hippuric acid in simulated urine for indexing toluene exposure with high selectivity, sensitivity and fast response. Dalton Trans 2021;50:553–61.
[20] Chen SY, Cheng SJ, Zhao L, Sun CY, Qin C, Su ZM. Self-assembly of zirconocene-based metal–organic capsules: the structure, luminescence sensing of Fe^{3+} and iodine capture. New J Chem 2020;44:21255–60.
[21] Wu Y, Zhong YY, Kang WY, Liu YW, Yang TT, Zhou M, et al. Two new luminescent Cd(II)-based coordination polymers by regulating the asymmetrical tetracarboxylate and auxiliary ligands displaying high sensitivity for Fe^{3+} and CrO_4^{2-}. CrystEngComm 2021;23:3460–6.
[22] Chuasaard T, Thammakan S, Semakul N, Konno T, Rujiwatra A. Structure and photoluminescence of two-dimensional lanthanide coordination polymers of mixed phthalate and azobenzene dicarboxylate. J Mol Struct 2022;1251:131940.
[23] Zhang X, Zhong FY, Liu J, Xu H, Gao JK, Xu SQ. A new three-dimensional metal-organic framework based on dinuclear rare earth cluster and olsalazine. Z Anorg Allg Chem 2019;645:1267–70.
[24] Sheldrick GM. SHELXT–integrated space-group and crystal-structure determination. Acta Crystallogr A Found Adv 2015;71:3–8.
[25] Sheldrick GM. Crystal structure refinement with SHELXL. Acta Crystallogr C Struct Chem 2015;71:3–8.
[26] Liu JJ, Lu YW, Lu WB. Photochromism and hydrochromism of three two-dimensional coordination polymers constructed from a carboxybenzyl viologen ligand. Dyes Pigments 2020;182:108631.
[27] Hao XY, Wang Y, Guan L, Guo YT. Four N-Heterocyclic carboxylate-phenolate coordination compounds: syntheses, structures, and fluorescent properties. Indian J Heterocycl Chem 2025;35:25–36.
[28] Guan L, Wang Y, Jin HZ, Yin PP. A new route for the syntheses of coordination polymers using magnetic influence: syntheses, crystal structures and fluorescence properties. IUCrJ 2023;10:671–7.
[29] Blatov VA, Shevchenko AP, Proserpio DM. Applied topological analysis of crystal structures with the program package ToposPro. Cryst Growth Des 2014;14:3576–86.
[30] Wang J, Zhou SH, Chen C, Lu L, Li BH, Hu WX, et al. Two new uncommon 3D cobalt-based metal organic frameworks: temperature induced syntheses and enhanced photocatalytic properties against aromatic dyes. Dyes Pigments 2021;187:109068.
[31] Niu YF, Cui LT, Han J, Zhao XL. Solvent-mediated secondary building units (SBUs) diversification in a series of Mn(II)-based metal-organic frameworks (MOFs). J Solid State Chem 2016;241:18–25.
[32] Wang LB, Wang JJ, Yue EL, Li JF, Tang L, Wang X, et al. Luminescent Zn(II) coordination polymers for highly selective detection of triethylamine, nitrobenzene and tetracycline in water systems. Dyes Pigments 2022;197:109863.

[33] Liu WH, Qiao JY, Gu JM, Liu YL. Hydrogen-bond-connected 2D Zn-LMOF with fluorescent sensing for inorganic pollutants and nitro aromatic explosives in the aqueous phase. Inorg Chem 2023;62:1272–8.
[34] Wei WW, Zhang X, Lu LP, Feng SS. Novel 2D isomorphic lanthanide complexes based on a bifunctional 5-(pyridin-3-yloxy)isophthalic acid: synthesis, structure, fluorescence and magnetic properties. CrystEngComm 2022;24:6204–14.
[35] Yu HH, Chi JQ, Su ZM, Li X, Sun J, Zhou C, et al. A water-stable terbium metal–organic framework with functionalized ligands for the detection of Fe^{3+} and $Cr_2O_7^{2-}$ ions in water and picric acid in seawater. CrystEngComm 2020;22:3638–43.
[36] Liu L, Li JM, Wang HJ, Zhang MD, Xi Y, Xu J, et al. Study on fluorescence recognition of Fe^{3+}, $Cr_2O_7^{2-}$ and p-nitrophenol by a cadmium complex and related mechanism. Molecules 2023;28:1848.
[37] Lin JF, Lin HY, Liu Y, Lu JJ, Wang X. Four new cobalt(II)/zinc(II) complexes derived from the naphthalene-bridging bis(pyridyl)-bis(amide) ligand: fluorescence sensing Fe^{3+} ions and CrO_4^{2-} anions, photocatalytic degrading dyes. J Solid State Chem 2022;307:122869.
[38] Otero-Fuentes GM, Sánchez-Mendieta V, Sánchez-Ruiz A, Morales-Luckie RA, Martínez-Otero D, Jaramillo-García J, et al. Highly selective ratiometric sensors for Pb^{2+} based on luminescent Zn(II)-coordination polymers with thiophenedicarboxylate. crystal structures and spectroscopic studies. J Fluoresc 2025;35:3449–59.
[39] Li Z, Zhan ZY, Hu M. A luminescent terbium coordination polymer as a multifunctional water-stable sensor for detection of Pb^{2+} ions, PO_4^{3-} ions, $Cr_2O_7^{2-}$ ions, and some amino acids. CrystEngComm 2020;22:6727–37.
[40] Nguyen VC, Chiang WH, Wu KCW. Water- and thermal-stable silver-based photoluminescent metal–organic coordination polymer for highly selective lead ion sensing. Bull Chem Soc Jpn 2019;92:1430–5.
[41] Xian GX, Chen YQ, Wang YH, Wan XY, Li YW, Wang HW, et al. Multifunctional sensing activities toward heavy metals of three luminescent complexes: effect of N-donor coligands and sensing medium. Dyes Pigments 2021;190:109291.
[42] Li L, Chen Q, Niu ZG, Zhou XH, Yang T, Huang W. Lanthanide metal–organic frameworks assembled from a fluorene-based ligand: selective sensing of Pb^{2+} and Fe^{3+} ions. J Mater Chem C 2016;4:1900–5.
[43] Sun XC, Li CX, Meng XG, Wang DJ, Zheng CY. A highly thermal and pH-stable fluorescence sensor for rapid detection of Hg^{2+}, Fe^{3+}, and tetracycline in aqueous solutions. CrystEngComm 2023;25:4531–8.
[44] Di M, Shen JW, Cui Z, Zhang XY, Zhang JP. Assembly of metal–organic frameworks based on 4-connected 3,3′,5,5′-azobenzenetetracarboxylic acid: structures, magnetic properties, and sensing of Fe^{3+} ions. New J Chem 2019;43:4226–34.
[45] Kim S, Kwak J, Lee SY. Optical sensing of copper(II) ions using a biofunctional bolaamphiphile self-assembly: selective binding of copper(II) ions to tyrosine moieties. Sens Actuators, B 2014;203:483–9.
[46] Molina MJ, Dobado JA, Melchor S. Structural and electronic effects of the interaction of metal cations with benzene. J Mol Struct Theochem 2002;589–590:337–47.
[47] Wang L, Tu BT, Xu W, Fu Y, Zheng YQ. Uranyl organic framework as a highly selective and sensitive turn-on and turn-off luminescent sensor for dual functional detection arginine and MnO_4^-. Inorg Chem 2020;59:5004–17.
[48] Ma ZL, Shi JY, Wang MC, Tian L. Lanthanide−organic complex with uncoordinated Lewis basic triazolyl sites as multi-responsive sensor for nitrobenzene, Cu^{2+} and MnO_4^-. Dyes Pigments 2021;185:108930.
[49] Mohan B, Ma SX, Kumar S, Yang Y, Ren P. Tactile sensors: hydroxyl decorated silver metal–organic frameworks for detecting $Cr_2O_7^{2-}$, MnO_4^-, humic acid, and Fe^{3+} ions. ACS Appl Mater Interfaces 2023;15:17317–23.
[50] Ma JJ, Liu WS. Effective luminescence sensing of Fe^{3+}, $Cr_2O_7^{2-}$, MnO_4^- and 4-nitrophenol by lanthanide metal–organic frameworks with a new topology type. Dalton Trans 2019;48:12287–95.
[51] Li B, Yan QQ, Yong GP. A new porous coordination polymer reveals selective sensing of Fe^{3+}, $Cr_2O_7^{2-}$, CrO_4^{2-}, MnO_4^- and nitrobenzene, and stimuli-responsive luminescence color conversions. J Mater Chem C 2020;8:11786–95.
[52] Zhang JF, Tao XY, Wang SX, Yue YL, Yin DJ, Zhang C. Microstructural modulation of isomorphic luminescent coordination polymers to achieve sensing effect transformation. Inorg Chem 2025;64:7797–805.
[53] Yang YF, Li DC, Qie SW, Su S, Hu M. Composite Eu@Cd-CP as a fluorescent probe for the detection of some food additives. Spectrochim Acta, Part A 2024;317:124401.
[54] Li D, Qie S, Mu Z, Yang Y, Hu W, Xu R, et al. An Eu coordination polymer: its single-crystal transformation synthesis, fluorescence detection of melamine, and proton conductivity. Inorg Chem 2025;64:5672–81.
[55] Liu YJ, Gao R, Liu XC, Zheng JH, Wu X. High-efficiency fluorescent coordination polymer nanoparticles Co-doped with Ce^{3+}/Tb^{3+} ions for curcumin detection. Microchim Acta 2023;190:354.
[56] Li DC, Yang YF, Su S, Jia YJ, Xing HW, Hu M. A Eu coordination polymer sensor for the detection of tartrazine, folic acid, and amino acids. Microchem J 2024;199:109995.
[57] Wang YN, Xu H, Wang SD, Feng WY, Mo Y, Bai JT, et al. 3D Zn(II)-based coordination polymer: synthesis, structure and fluorescent sensing property for nitroaromatic compounds. Spectrochim Acta, Part A 2023;297:122708.
[58] Zhao XY, Wang J, Yang QS. Highly sensitive and selective sensing of ascorbic acid in water with a three-dimensional terbium(III)-based coordination polymer. Euro Poly J 2021;160:110771.
[59] Vinita Nirala NR, Tiwari M, Prakash R. A nanoporous palladium(II) bridged coordination polymer acting as a peroxidase mimic in a method for visual detection of glucose in tear and saliva. Microchim Acta 2018;185:245.
[60] Zhao XY, Yang QS, Wang J, Fu DL, Jiang DK. A novel 3D coordination polymer constructed by dual-ligand for highly sensitive detection of purine metabolite uric acid. Spectrochim Acta, Part A 2021;262:120065.
[61] Zhao YF, Zeng H, Zhu XW, Lu WG, Li D. Metal–organic frameworks as photoluminescent biosensing platforms: mechanisms and applications. Chem Soc Rev 2021;50:4484–513.
[62] Wang YN, Wang SD, Fan Y, Yu L, Zha RH, Liu LJ, et al. A dual-chemosensor based on Ni-CP: fluorescence turn-on sensing toward ascorbic acid and turn-off sensing toward acetylacetone. J Fluoresc 2022;243:118680.
[63] He YH, Ghosh MK, Ma RM, Lu L, Cai SL, Afzal M, et al. A tetrahedral zinc(II) coordination polymer: synthesis, characterisation, and application in ascorbic acid fluorescence sensing. J Mol Struct 2025;1322:140530.
[64] Wang YN, Wang SD, Dong PH, Wang F, Dou WQ, Lu SQ, et al. A dual-functional Co (II) coordination polymer luminescent sensor: turn-off sensing acetylacetone and rare turn-on detection of ascorbic acid. Inorg Chim Acta 2021;527:120546.
[65] Wang YN, Wang SD, Sun Y, Yang QF, Wang SY, Wen LM, et al. Dual-responsive luminescent sensitivities of a 3D Co-CP with turn-on and ratiometric sensing toward ascorbic acid and turn-off detecting acetylacetone. J Solid State Chem 2022;315:123463.
[66] Zhao Y, Zeng H, Zhu XW, Lu W, Li D. Metal–organic frameworks as photoluminescent biosensing platforms: mechanisms and applications. Chem Soc Rev 2021;50:4484–513.